Lifetime measurement of ${}^{5}_{\Lambda}$He hypernucleus

Satoru Kameoka

Abstract

We performed hypernuclear decay experiment of ${}^{5}_{\Lambda}\mathrm{He}$ at 12 GeV Proton Synchrotron of High Energy Accelerator Research Organization(KEK) from year 2000 to 2001. It was aimed to measure the lifetime and the partial decay width of ${}^{5}_{\Lambda}\mathrm{He}$ with high statistics to provide conclusive information to the study of hypernuclear structure and decay mechanism. The partial decay width is significant observable to establish the existence of the repulsive core, which has been theoretically proposed as an unique nature of Λ-nucleus potential. Hypernuclear formation was successfully identified owing to high resolution spectrometer SKS. The present work measured the lifetime of ${}^{5}_{\Lambda}\mathrm{He}$ using the data accumulated in year 2000 and gave preliminary result as 282^{+21}_{-19} ps, which was a little longer(1.3σ level) than old data with the same order of the accuracy. The proton energy spectrum from non-mesonic decay of ${}^{5}_{\Lambda}\mathrm{He}$ was also obtained with considerable good precision.

Contents

Chapter 1

Introduction

1.1 Weak decay of hypernuclei

1.1.1 Outline

Hypernucleus is a unique nucleus which binds hyperon such as Λ, Σ and Ξ. Excitation spectra of Λ hypernuclei have been measured in many experiments to reveal single-particle nature of Λ. Quantum states of deeply bound nucleus were observed for the first time by hypernuclear experiments since Λ is allowed to occupy low-lying orbits filled with proton or neutron.

The difference and analogy between Λ-N interaction and N-N interaction have been studied so as to probe the mechanism of the nuclear force, which is not understood well yet. Hypernuclear decay is one of the interesting processes for such a purpose. Λ hypernuclei decay via strangeness changing weak interaction between hadrons. Mesonic decay of Λ is characterized by pion emission, and expressed as

$$\Lambda \to p + \pi^- + 37.8 \text{ MeV} \qquad (63.9\%) \;, \tag{1.1}$$

$$\Lambda \to n + \pi^0 + 41.1 \text{ MeV} \qquad (35.8\%) \;. \tag{1.2}$$

Quoted branching ratio is known as one of the important illustration of $\Delta I = 1/2$ rule. Released energy via mesonic decay is not large enough to excite the nucleon above Fermi surface except for light hypernuclei. In heavier hypernuclei, therefore, it is replaced by the other decay process, called non-mesonic decay:

$$\Lambda + p \;\to\; n + p + 176 \text{ MeV} \;, \tag{1.3}$$

$$\Lambda + n \;\to\; n + n + 176 \text{ MeV} \;. \tag{1.4}$$

Energetic nucleon pair whose momentum is about 400 MeV/c is emitted via non-mesonic decay. Two-nucleon-induced non-mesonic decay represented as $\Lambda NN \to NNN$ is also predicted theoretically, but not well established yet. Therefore total decay width(Γ_{tot}) is described by:

$$\Gamma_{tot} \equiv 1/\tau = \Gamma_{\mathrm{m}} + \Gamma_{\mathrm{nm}} \;, \tag{1.5}$$

$$\Gamma_{\mathrm{m}} = \Gamma_{\pi^-} + \Gamma_{\pi^0} \;, \tag{1.6}$$

$$\Gamma_{\mathrm{nm}} = \Gamma_p + \Gamma_n + (\Gamma_{2N}) \;, \tag{1.7}$$

where τ is lifetime of the hypernuclei, and $\Gamma_{\pi^-(\pi^0)}$ is the partial decay width of $\pi^-(\pi^0)$ mesonic decay, $\Gamma_{p(n)}$ is that of proton-(neutron-)induced non-mesonic decay, and Γ_{2N} is that of the two-nucleon-induced non mesonic decay.

1.1.2 Mesonic decay

Hyperon-nucleon scattering experiment is so difficult that hypernuclei has been mainly studied for the purpose of extracting the nature of Λ-nucleon force.

Effective Λ-nucleus potential was theoretically calculated and the existence of the repulsive core in s-shell hypernuclei has been discussed. It was obtained by folding the Λ-nucleon interaction which was based on well-understood free Λ decay. Hypernuclear decay provides significant information to evaluate the validity of the potential, since the decay width depends on the extent of the overlap between the Λ wave function and the nucleon. Motoba *et al.*[14] and Kumagai-Fuse *et al.*[13] calculated partial decay width of s-shell hypernuclei for two different potentials:one has simple attractive form as a conventional nuclear single-particle potential, while the other has central repulsion. Both of them were constructed to reproduce experimentally observed Λ binding energy.

Recently pionic decay rate of ${}^{4}_{\Lambda}\mathrm{H}$ and ${}^{4}_{\Lambda}\mathrm{He}$ were independently measured by Outa *et al.* [22] and Zeps *et al.* [24] to provide improved data. They are listed in Table 1.1 with theoretical estimation by Kumagai *et al.* The Isle potential has two-range gaussian form with the central repulsion, whereas SG has a single-gaussian form (see Figure 1.1)[13]. Isle potential seems preferred, but it is only by 1 sigma level. Improved error level measurement of mesonic decay width are necessary so as to establish the existence of inner repulsive core in the Λ-nucleus potential.

Szymanski's data for ${}^{5}_{\Lambda}\mathrm{He}$ is also displayed, which have as large as 25% error even for π^- induced decay width. Figure 1.2 (left) shows the excitation spectra of ${}^{6}\mathrm{Li}(K^-,\pi^-){}^{6}_{\Lambda}\mathrm{Li}$ reaction used to give that result. It is noted that serious background from decay of beam kaon caused large ambiguity in evaluating hypernuclear yield and extracting the branching ratio. In contrast, the ground state is clearly identified not only in coincident spectrum but also in inclusive one in Figure 1.2 (right) obtained by ${}^{6}\mathrm{Li}(\pi^+,K^+){}^{6}_{\Lambda}\mathrm{Li}$ experiment performed at KEK(High Energy Accelerator Research Organization). Accordingly, (π^+,K^+) experiment is suitable for accurately measuring the branching ratio of hypernuclear decay.

Concerning the π^- decay width for A=5, theoretical calculation by Kumagai-Fuse shows about 30% difference between the SG potential and Isle potential, thus we hopefully need better than 10%-level measurement to distinguish these two.

For this purpose, we need to measure both of lifetime and π^- mesonic decay branching ratio for ${}^{5}_{\Lambda}\mathrm{He}$ with $\sim$5% error. The lifetime of ${}^{5}_{\Lambda}\mathrm{He}$ was already reported with 8% error, but this need to be improved another factor of two.

1.1.3 Non-mesonic decay

In early stage, the mechanism of non-mesonic decay process was studied with natural extension of mesonic decay, assuming virtual pion exchange between weak $\Lambda N\pi$ vertex and strong $NN\pi$ vertex depicted in Figure 1.3[2, 12]. However this one pion exchange(OPE) model resulted in showing one order of magnitude smaller Γ_n/Γ_p ratio than existing experimental data.

Many theoretical works were developed to solve this puzzle. It is been pointed out that the contribution of the short range force need to be taken into account in non mesonic decay process, which is characterized by the large momentum transfer. The heavier meson and two pion exchange potential were discussed[**?**, 20], but their

decay ratio	Outta *et al.*	Zeps *et al.*	Szymanski *et al.*	SG	Isle
${}^{4}_{\Lambda}$H					
$\Gamma_{\pi^0}/\Gamma_\Lambda$				0.16	0.19
$\Gamma_{\pi^-}/\Gamma_\Lambda$	$1.00^{+0.18}_{-0.15}$			0.93	0.88
$\Gamma_{\pi^- {}^4\mathrm{He}}/\Gamma_\Lambda$	$0.69^{+0.12}_{-0.10}$			0.71	0.61
$\Gamma_{\pi^- {}^4\mathrm{He}}/\Gamma_\pi^-$	0.69 ± 0.02			0.76	0.69
${}^{4}_{\Lambda}$He					
$\Gamma_{\pi^0}/\Gamma_\Lambda$	0.53 ± 0.07	0.60 ± 0.08		0.51	0.49
$\Gamma_{\pi^-}/\Gamma_\Lambda$	0.33 ± 0.05	0.26 ± 0.03		0.25	0.31
$\Gamma_{\pi^0}/\Gamma_{\pi^-}$	1.59 ± 0.20	2.3 ± 0.4		2.02	1.59
${}^{5}_{\Lambda}$He					
$\Gamma_{\pi^0}/\Gamma_\Lambda$			0.18 ± 0.20	0.16	0.20
$\Gamma_{\pi^-}/\Gamma_\Lambda$			0.44 ± 0.11	0.31	0.40

Table 1.1: partial decay width of s-shell hypernuclei in units of free Λ decay width.

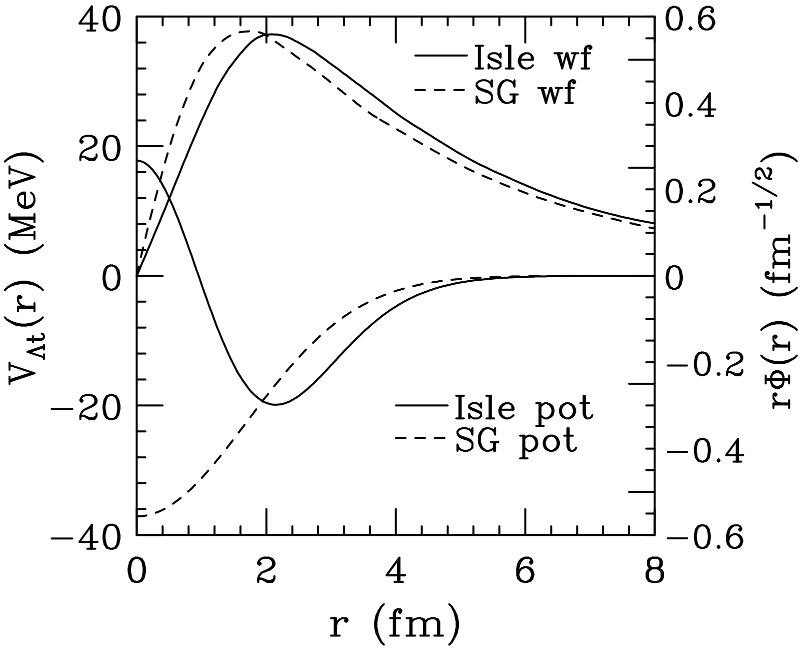

Figure 1.1: Λ-nucleus potential and Λ radial wave function for Isle(solid line) and SG(dotted line).

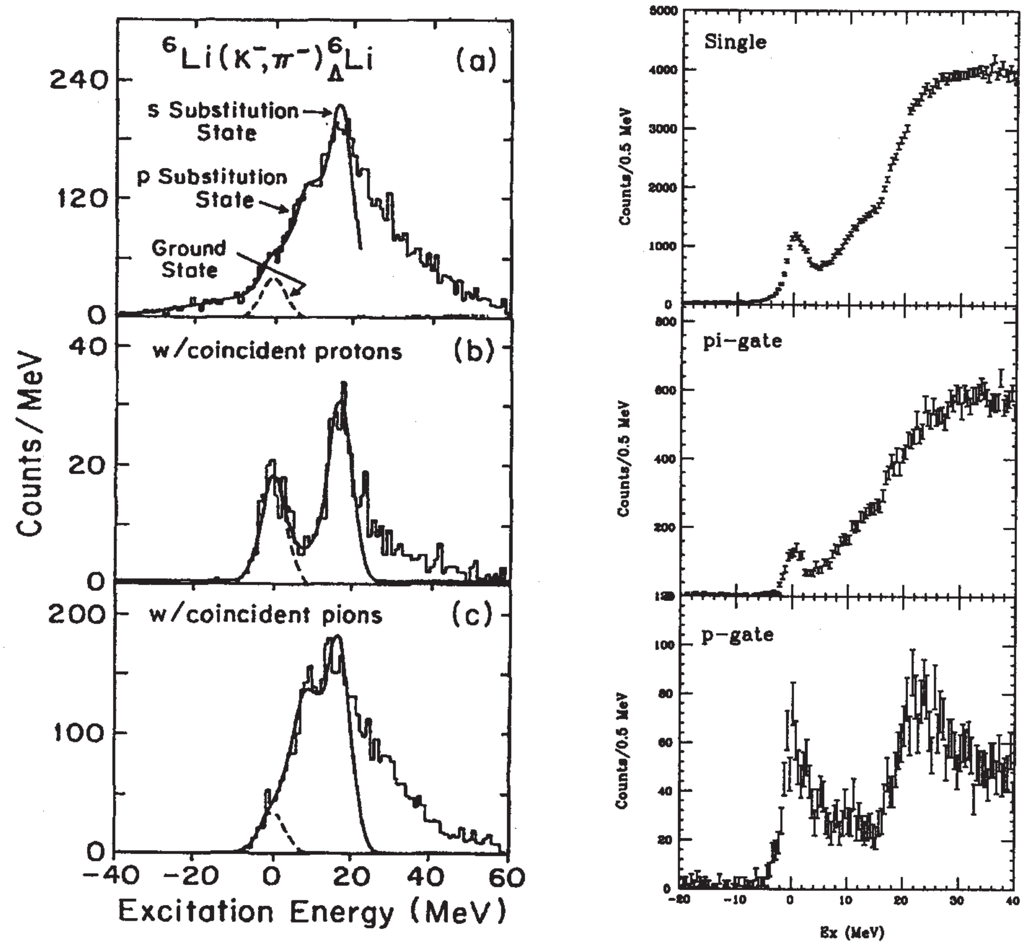

Figure 1.2: Comparison of excitation spectra of $^{6}\mathrm{Li}(K^{-},\pi^{-})^{6}_{\Lambda}\mathrm{Li}$ reaction[7] and $^{6}\mathrm{Li}(\pi^{+},K^{+})^{6}_{\Lambda}\mathrm{Li}$ reaction[10].

effect was found to be canceled and failed to solve the Γ_n/Γ_p puzzle. Oka treated the non-mesonic decay as a direct interaction between constituent quarks[19]. This procedure tends to reproduce the experimental data to imply violation of $\Delta I = 1/2$ rule in non-mesonic decay.

However it should be noted that old experimental data has too large statistical error to attribute the discrepancy to the theoretical framework. Owing to recent progresses in the experimental technique, decay product of hypernuclei came to be measured with high statistics.

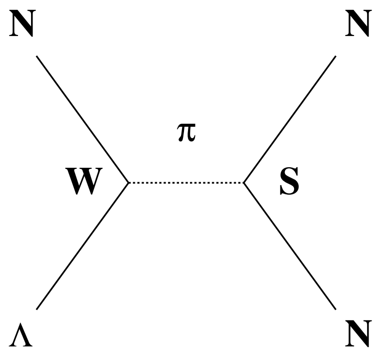

Figure 1.3: Feynman diagram of simple OPE model of non-mesonic decay. Vertices W and S depict weak and strong interaction, respectively.

KEK-PS E307

Lifetime and partial decay width, Γ_p, Γ_{π^-} were measured for ${}^{12}_{\Lambda}$C and other heavier hypernuclei with high precision in KEK-PS(Proton Synchrotron) E307 experiment, which was performed in 1995[5, 6, 16, 17]. Since pair nucleus generated via $\Lambda N \rightarrow NN$ process share almost all of released energy, their energy distributions are expected to have a peak around 70 MeV even though it is broadened reflecting Fermi motion of Λ and nucleon. Obtained proton energy spectrum showed no peak structure. That was supposed to be ascribed to FSI effect, which means the interaction between outgoing nucleon pair and spectator nucleon, or two-nucleon-induced non-mesonic decay. Ramos *et al.* calculated energy spectra and yield of proton and neutron from non-mesonic decay as a function of Γ_n/Γ_p[8]. The FSI effect was considered using an intranuclear cascade code. As shown in Figure 1.4, observed proton spectra were well explained by Ramos's calculation concerning their shapes, but the yield again concluded remarkably larger Γ_n/Γ_p than theoretical estimation even for the calculation including two-nucleon-induced non-mesonic decay[32]. Table 1.2 compares the derived Γ_n/Γ_p ratio for ${}^{12}_{\Lambda}$C and ${}^{29}_{\Lambda}$Si with recent theoretical calculations. Other hypernuclear data measured by previous experiments are also displayed.

However the Γ_n/Γ_p ratio was derived only from the protons, and large ambiguity of "missing number measurement" cannot be excluded. Therefore a direct neutron measurement had been awaited.

KEK-PS E369

The KEK-PS E369 measured neutrons from decay of ${}^{12}_{\Lambda}$C and ${}^{89}_{\Lambda}$Y, and drastically improved the past experiment[7] in statistic and quality. The neutron energy spectroscopy has advantage to that of proton especially at low energy region since it

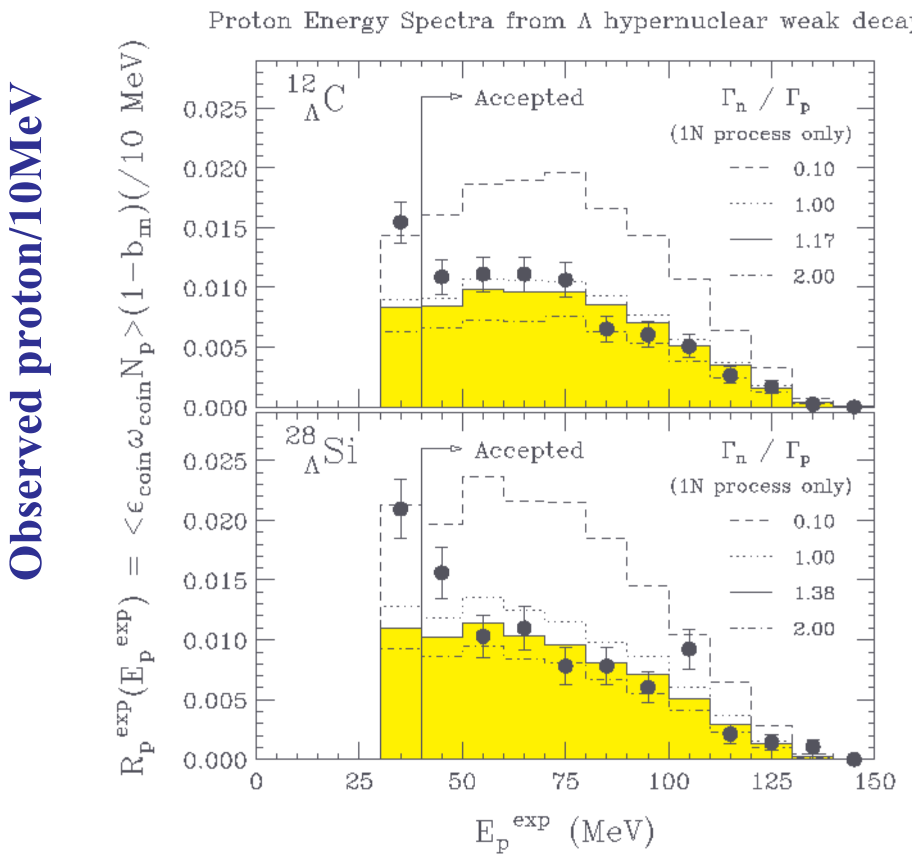

Figure 1.4: Proton energy spectra for $^{12}_{\Lambda}$C(top) and $^{28}_{\Lambda}$Si(bottom) measured by E307(closed circles). The vertical axes were normalized to the number of protons per hypernuclear decay. Simulation results where FSI was considered were superimposed. The histogram with solid lines gave the best fit.

Hypernuclei	Experiment		Theory
	$1N$ only	$1N$ and $2N$	
$^{5}_{\Lambda}$He	0.93 ± 0.55[7]	—	0.489[34]
$^{11}_{\Lambda}$B	$2.16 \pm 0.58^{+0.45}_{-0.95}$[4]	—	0.084[9]
$^{12}_{\Lambda}$C	$1.17^{+0.09+0.20}_{-0.08-0.18}$[32]	$0.96^{+0.10+0.22}_{-0.09-0.21}$[32]	0.31[21], 0.53[35]
$^{28}_{\Lambda}$Si	$1.38^{+0.13+0.27}_{-0.11-0.25}$[32]	$1.18^{+0.14+0.30}_{-0.13-0.28}$[32]	0.34[21]

Table 1.2: Experimental data and theoretical estimation of Γ_n/Γ_p ratio for several hypernuclei. For $^{12}_{\Lambda}$C and $^{29}_{\Lambda}$Si, Γ_n/Γ_p was derived with two ways: one considered only two-body decay process($1N$ only) and the other considered the contribution of three-body decay process ($1N$ and $2N$).

is free from energy loss in production target and detectors. The obtained neutron spectra showed no peak structure, and strongly favored remarkable contribution of two-nucleon-induced non-mesonic decay process in comparison with Ramos's estimation (see Figure 1.5). Furthermore neutron yield per non-mesonic decay of ${}^{12}_{\Lambda}$C was about 0.81/0.69 with energy threshold 30/40 MeV, which is much less than the value derived from that of proton in E307 and Ramos's calculation (see Figure 1.6). It is also possible that this contradiction is caused by the theoretical underestimation of the FSI effect.

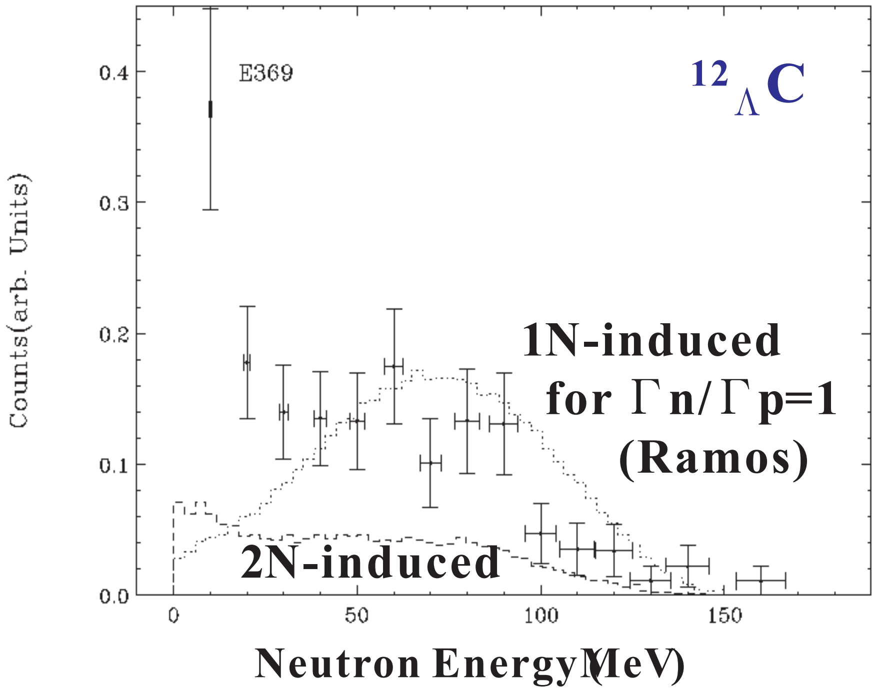

Figure 1.5: Neutron spectrum obtained by E369[33] is compared to Ramos's calculation assuming $\Gamma_n/\Gamma_p = 1$, which is exhibited by solid line[8]. The calculation was performed for ether one-nucleon-induced non-mesonic decay and two-nucleon induced one, where the FSI effect was taken into account by Monte Carlo simulation. The experimental result resembles the latter estimation. Sizable contribution from two-nucleon-induced non-mesonic decay or theoretical underestimation of FSI is implied consequently.

1.2 The present experiment(KEK-PS E462)

1.2.1 Lifetime and partial decay width

The KEK-PS E462 experiment aimed to measure the lifetime and partial decay width of ${}^{5}_{\Lambda}$He and provide much more refined information to hypernuclear study than previous experiments. High intensity pion beam was used to produce the hypernuclei via (π^+, K^+) reaction with high statistics. High resolution spectrometer SKS was employed to reconstruct hypernuclear mass spectrum. The decay counter sensitive

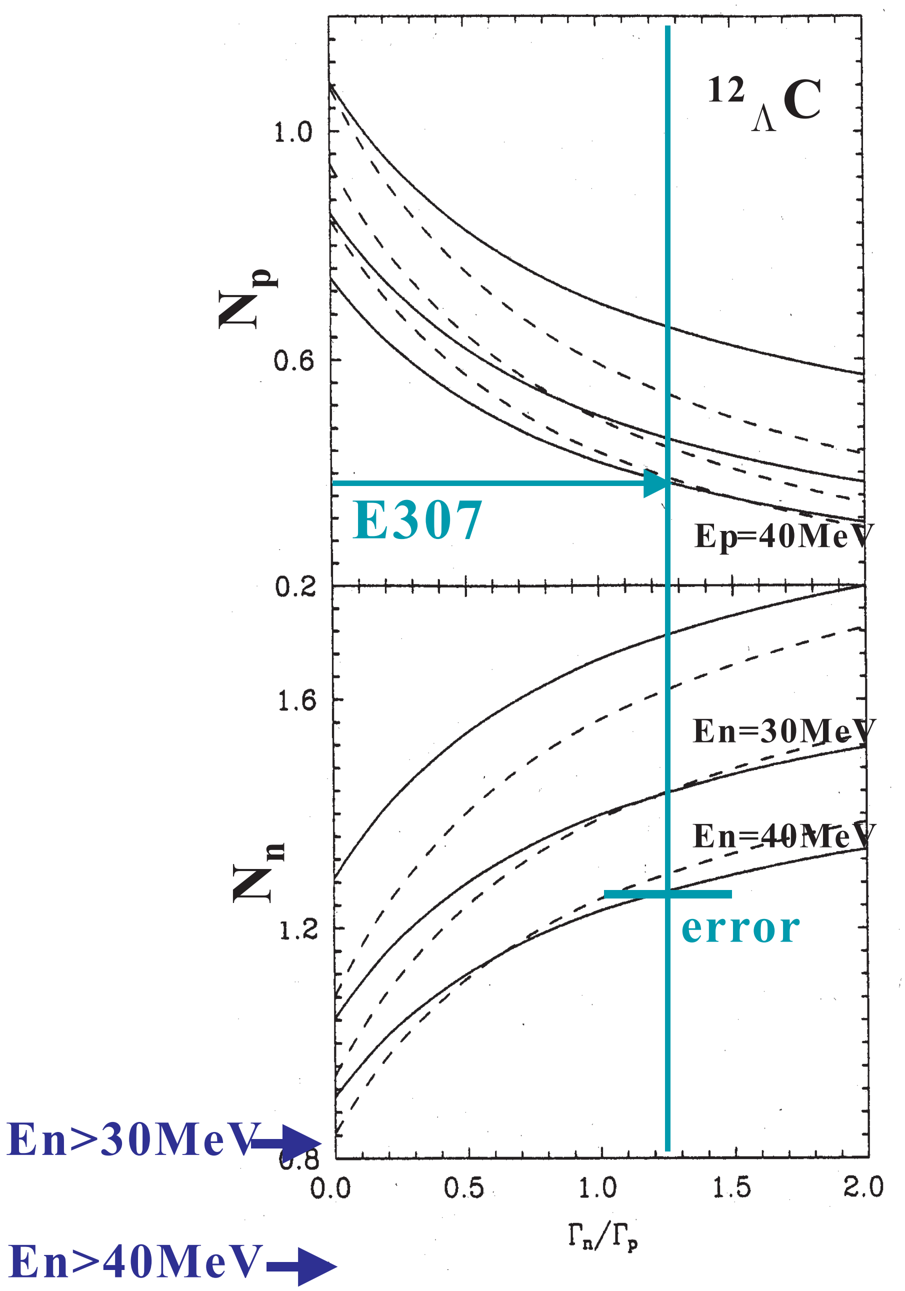

Figure 1.6: Proton and neutron yield per ${}^{12}_{\Lambda}C$ decay as a function of Γ_n/Γ_p calculated by Ramos. The Dashed lines correspond to considering only the $1N$-induced decay, while the solid lines include also the $2N$-induced one. Detection thresholds were set at 30 MeV or 40 MeV. The result of E307 infers the Γ_n/Γ_p ratio around 1.2, which is just intersection point of solid line and dotted line. The corresponding neutron number obtained by E369 fell far short from the extrapolated value for both 30 MeV and 40 MeV of the threshold.

to both charged and neutral particle was installed to detect proton, pion and neutron emitted via weak decay of the hypernuclei. First timing counters were used for lifetime measurement with essetially same meshod to E307.

1.2.2 Γ_n/Γ_p ratio

The experimental setup was also optimized for the direct measurement of Γ_n/Γ_p ratio. The decay counter was arranged symmetrically around ^{6}Li target so as to catch the nucleon pair selectively. As mentioned above, two outgoing nucleon have near to 180 degree opening angle and clear energy correlation. Measuring the correlated quantities, it becomes possible to select $\Lambda N \to NN$ events with high accuracy. An additional decay arm was installed to 90 degree direction for studying three body final states arise from the FSI or two-nucleon-induced non-mesonic decay. The yields of coincident nucleon pair are expressed as:

$$N(nn\text{-pair coin.}) = N(\Lambda n \to nn) \times (\Omega_n \times \Omega_n)_{\text{av.}} \times \varepsilon_n^2 \times (1 - R_{FSI}) , \quad (1.8)$$

$$N(np\text{-pair coin.}) = N(\Lambda p \to np) \times (\Omega_p \times \Omega_n)_{\text{av.}} \times \varepsilon_n \times \varepsilon_p \times (1 - R_{FSI}) , \quad (1.9)$$

where $(\Omega_n \times \Omega_n)_{\text{av.}}/$ $(\Omega_p \times \Omega_n)_{\text{av.}}$ and $\varepsilon_n/\varepsilon_p$ denote averaged acceptance of decay counter for n-n/n-p pair and detection efficiencies of neutron/proton, respectively. A factor R_{FSI} represents the reduction ratio due to the FSI effect. Consequently, the ratio between neutron and proton stimulated non-mesonic decay rates can be derived as:

$$\frac{\Gamma_n}{\Gamma_p} = \frac{N(nn\text{-pair coin.})}{N(np\text{-pair coin.})} \times \frac{\varepsilon_p}{\varepsilon_n} . \quad (1.10)$$

The FSI factor is canceled out due to the charge symmetry between proton and neutron. This experiment is epoch-making in the respect that Γ_n/Γ_p is determined without theoretical ambiguity of the FSI effect. It's noted that the lifetime should be simultaneously measured to extract not only the branching ratio but also the partial decay width which is to be compared with theoretical calculation. Determination of Λ-nucleus potential is also important for the study of non-mesonic decay, since theoretical estimation of non-mesonic decay width is highly depend on Λ-nucleus potential shape.

1.2.3 $^{5}_{\Lambda}$He hypernucleus

Hypernuclear experiments using $^{5}_{\Lambda}$He were performed at BNL[7] and KEK[10] in the past. It is known that $s_n^{-1}s_\Lambda$ and $p_n^{-1}s_\Lambda$ states of $^{6}_{\Lambda}$Li generated by ^{6}Li(K^-, π^-) or ^{6}Li(π^+, K^+) reaction decay into the ground state of $^{5}_{\Lambda}$He with a prompt proton emission as depicted in Figure 1.7.

1.3 Thesis composition

In this thesis the result of the lifetime analysis is reported as a part of our project, exclusive measurement of $^{5}_{\Lambda}$He. The experimental apparatus is explained in Chapter 2. In chapter 3 detail of the data analysis will be given. Results and further prospects are discussed in Chapter 4.

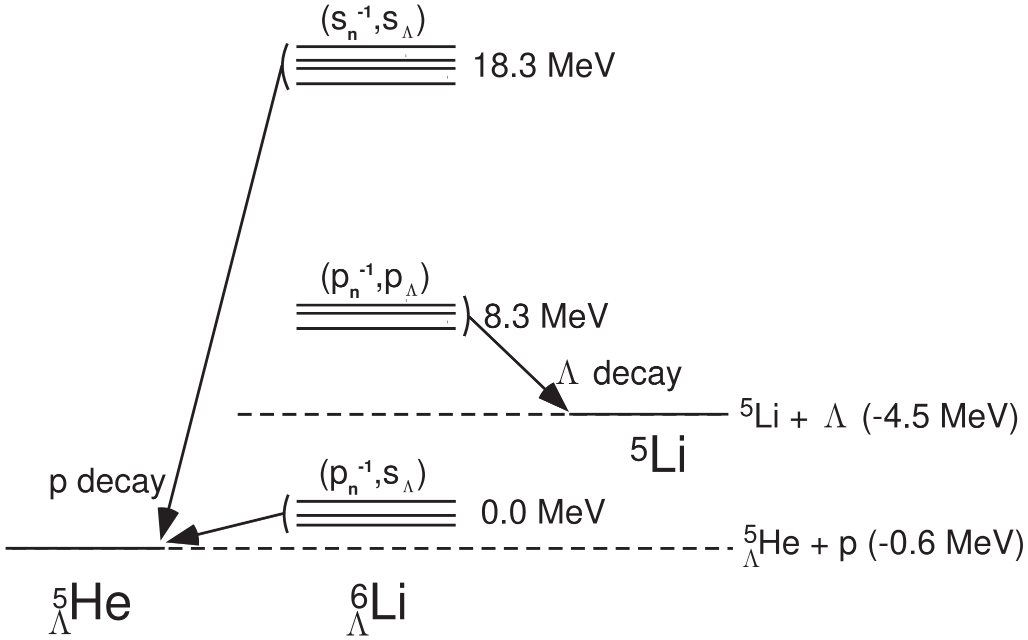

Figure 1.7: Deexcitation process of $^6_\Lambda$Li

Chapter 2

Experimental setup

2.1 K6 beamline

Pion beam supplied by K6 beam line (Figure 2.1) of KEK-PS was used to produce hypernuclei. Pion was generated by bombarding platinum target with 12 GeV proton beam. and separated from the other kinds of charged particle by the electrostatic separator(DC separater). QQDQQ magnet system, which served as beam spectrometer, was placed at the terminal of the beamline (Figure 2.2). It is composed of one dipole magnet and four quadruple magnets. Beam momentum was set to the value around 1.05 GeV/c, where Λ formation cross section via (π, K) reaction grows maximum as shown in Figure 2.3. The (π^+, K^+) experiment requires high intensity beam to compensate for much smaller cross section than that of (K^-, π^-) reaction, although the capacity of data taking system is limited. Thus online trigger should be constructed by several kinds of counters in order to acquire data as effectively as possible. Gas Čerencov counter (GC) was employed to veto electron/positron mixed in beam. The hodoscopes BH1 (Figure 2.4) and BH2 are placed at the entrance and exit of QQDQQ magnet system, respectively, and create the beam trigger as a coincident hit of them with the timing which was not for proton contamination but for pion. To prevent gain deterioration of PMTs for BH1 and BH2, the voltage of the last three dynodes were retained by additional power supply (booster). Drift chambers (BDC1-4) were used to reconstruct beam trajectory. They have 2.5 mm spaced drift cells and as many as 12 planes which are arranged to have better horizontal position resolution for the operation under high rate beam (Figure 2.5). Each planes are shifted for size of a half cell against their partner to solve the left-right ambiguity (Figure 2.6). Typical beam intensity and ratio were 1.5×10^6 counts and 0.4 second, respectively, per repetition cycle of 3 seconds.

Momentum resolution	0.1%(FWHM)
Momentum bite	$\pm 3\%$
Maximum momentum	1.1 GeV/c
Bending angle	$60°$

Table 2.1: Design parameters of the beam spectrometer.

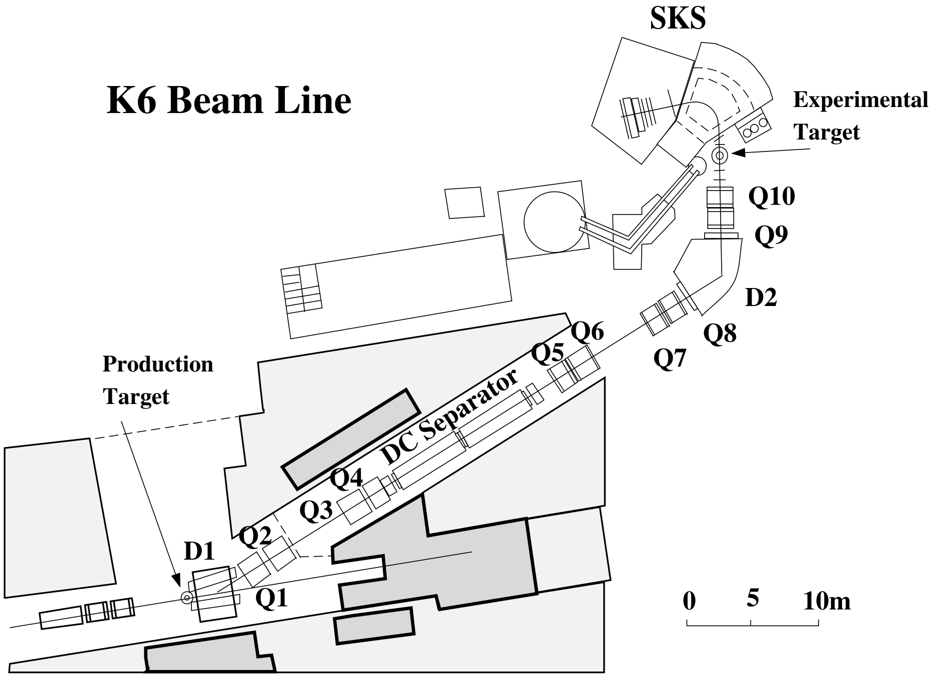

Figure 2.1: schematic view of k6 beamline.

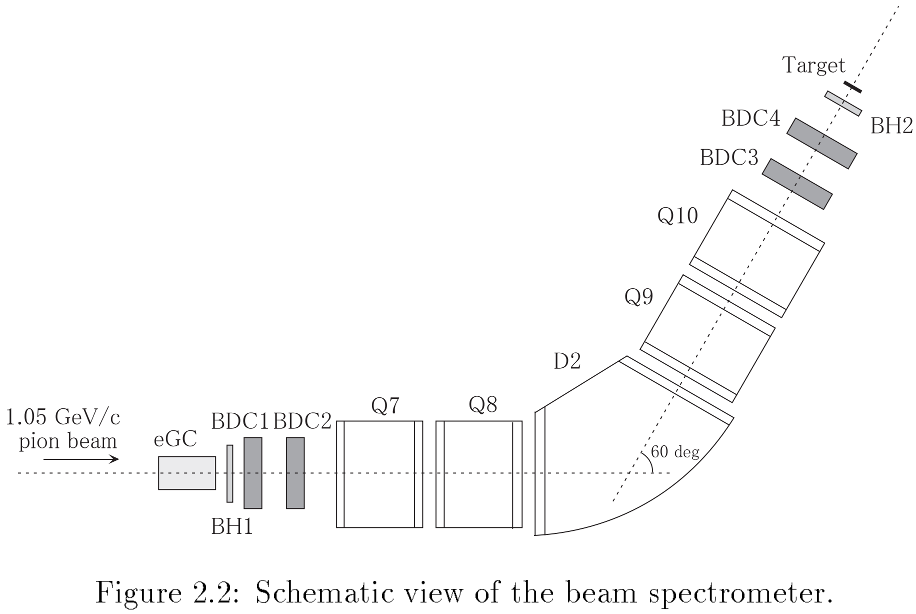

Figure 2.2: Schematic view of the beam spectrometer.

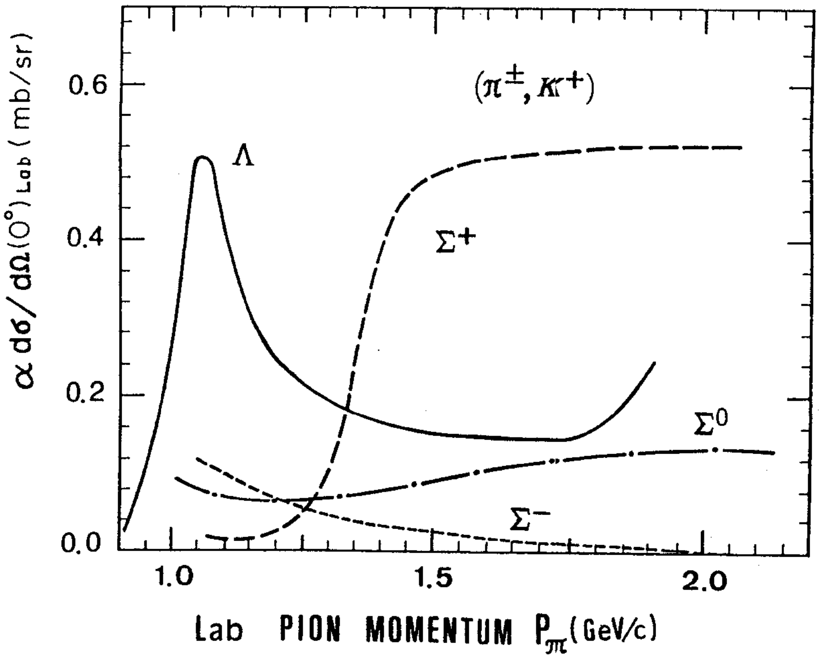

Figure 2.3: hyperon production cross section via (π, K) reaction as a function of projectile beam momentum.

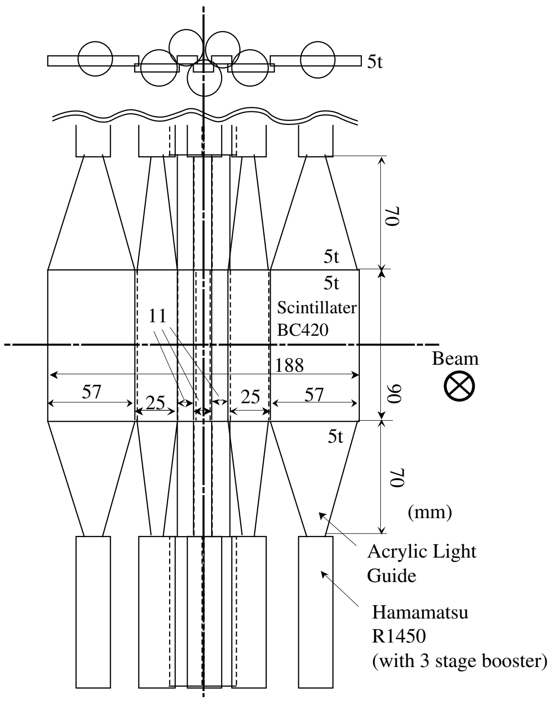

Figure 2.4: Schematic view of BH1.

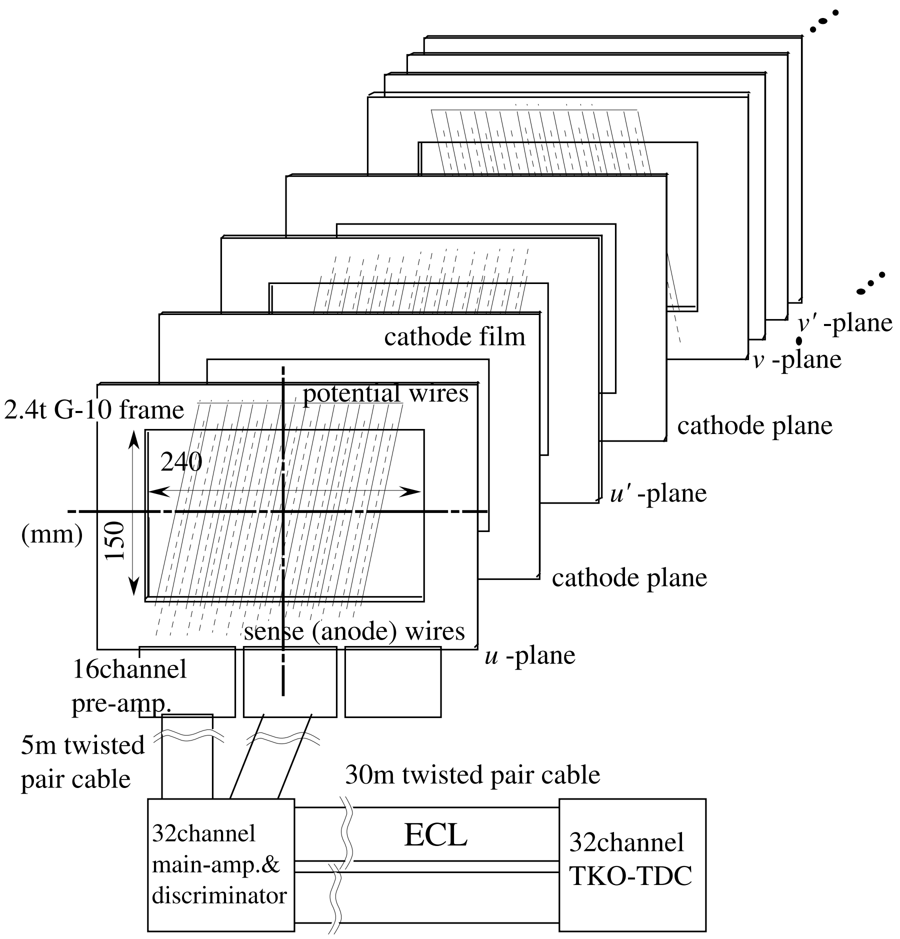

Figure 2.5: Structure and read-out system of BDCs.

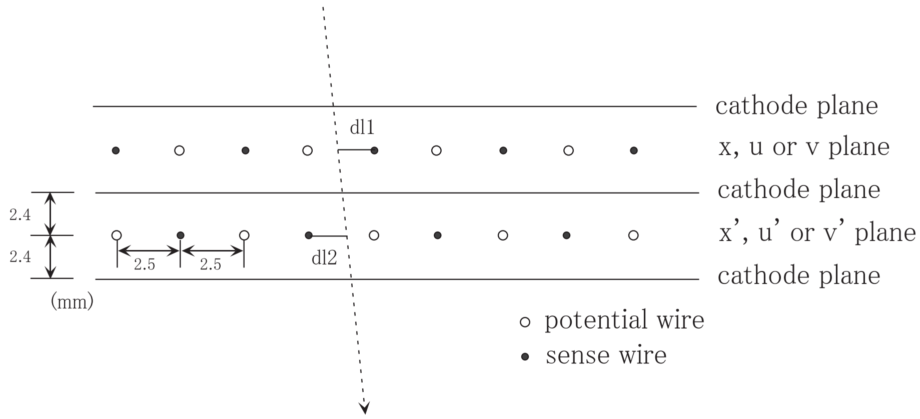

Figure 2.6: Cell structure of BDCs.

2.2 Scattered particle spectrometer(SKS)

Scattered particles were identified and tracked by the detector system located behind the experimental target. SKS(Super Conducting Kaon Spectrometer) simultaneously realized large acceptance and high momentum resolution. Figure 2.7 and Table 2.2 show a schematic view and parameters of SKS. It is designed to suppress the path length as short as possible to prevent kaon from decaying in flight. Scattered particle trigger is defined by TOF wall (Figure reftof) defines primary trigger for the scattered particle. Lucite Čerencov counter (LC) (Figure 2.9) and aerogel Čerencov counter (AC1 and AC2) (Figure 2.11) serve K/p separation and $\pi/K, p$ separation around the central momentum of SKS, respectively. As shown in Figure 2.10, High momentum protons also stimulate LC, which need to be cut in offline analysis. Drift chambers, SDC1/2 and SDC3/4 were installed at the entrance and exit of the SKS, respectively. SDC1/2 were also exposed to high rate beam, and they had essentially the same structure to BDCs. SDC3/4 had larger drift cells than the other chambers, and several number of field wires were added to make uniform electric field. SDC4 had six sense wires per cell and they were staggered by 200 μm to solve left-right ambiguity(Figure 2.12). Helium bags were put in the gap of the SKS and between SDC3 and SDC4 to reduce multiple scattering of charged particles. Specification of the hodoscopes and drift chambers are exhibited in Table 2.3 and Table 2.4, respectively.

Momentum resolution	0.1 % FWHM at 720 MeV/c
Maximum central momentum	1.1 GeV/c
Momentum bite	$\pm$ 10 %
Bending angle	100° for the central trajectory
Solid angle	100 msr
Flight path	$\sim$ 5 m for the central trajectory

Table 2.2: Design parameters of SKS.

Name	Sensitive area (cm)	PMT (Hamamatsu)	etc.
GC	$\phi 20 \times 29^{\mathrm{L}}$	R1584-02 $\times$ 1	Freon-12, n=1.00245
BH1	$19^{\mathrm{W}} \times 9^{\mathrm{H}} \times 0.5^{\mathrm{T}}$	R1450 $\times$ 14	7-segments, 3-stage-booster
TOF	$105^{\mathrm{W}} \times 100^{\mathrm{H}} \times 3^{\mathrm{T}}$	R1949 $\times$ 30	15-segments
AC1	$105^{\mathrm{W}} \times 120^{\mathrm{H}} \times 9^{\mathrm{T}}$	R1584-02 $\times$ 18	n=1.06
AC2	$140^{\mathrm{W}} \times 140^{\mathrm{H}} \times 12^{\mathrm{T}}$	R1584-02 $\times$ 20	n=1.06
LC	$140^{\mathrm{W}} \times 140^{\mathrm{H}} \times 4^{\mathrm{T}}$	H1949 $\times$ 28	14-segments, n=1.49

Table 2.3: Specifications of the trigger counters.

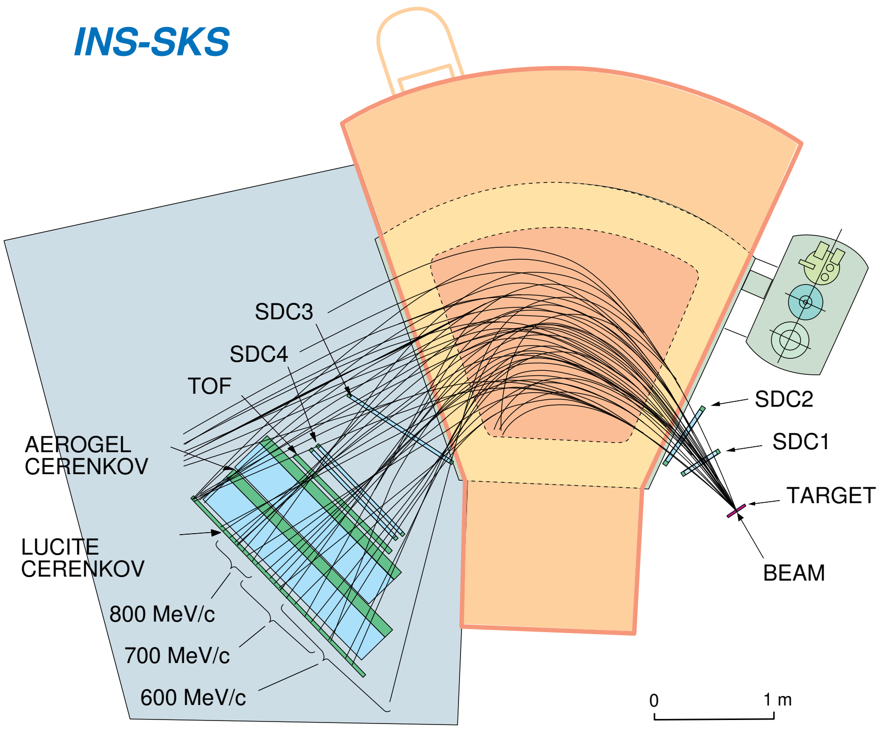

Figure 2.7: Schematic view of SKS

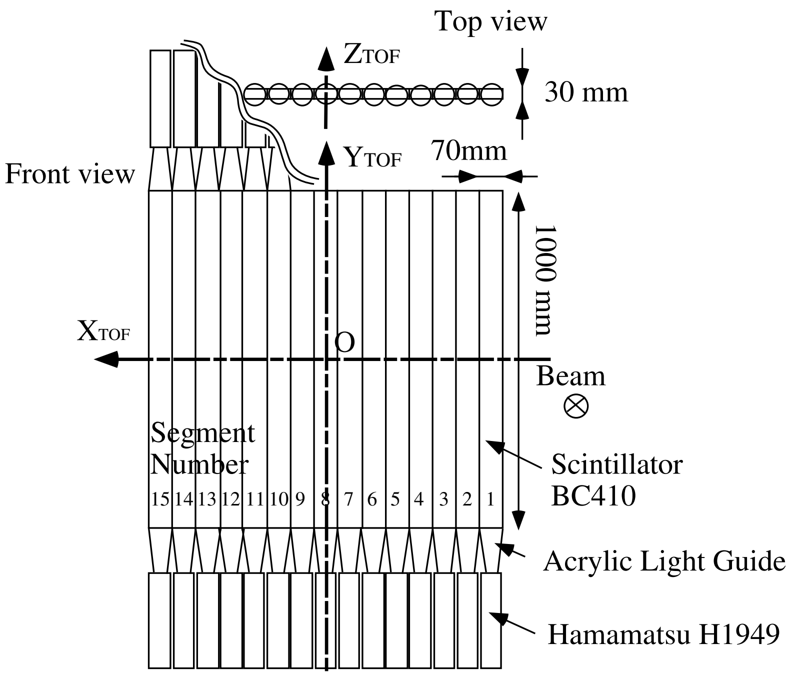

Figure 2.8: Schematic view of TOF wall

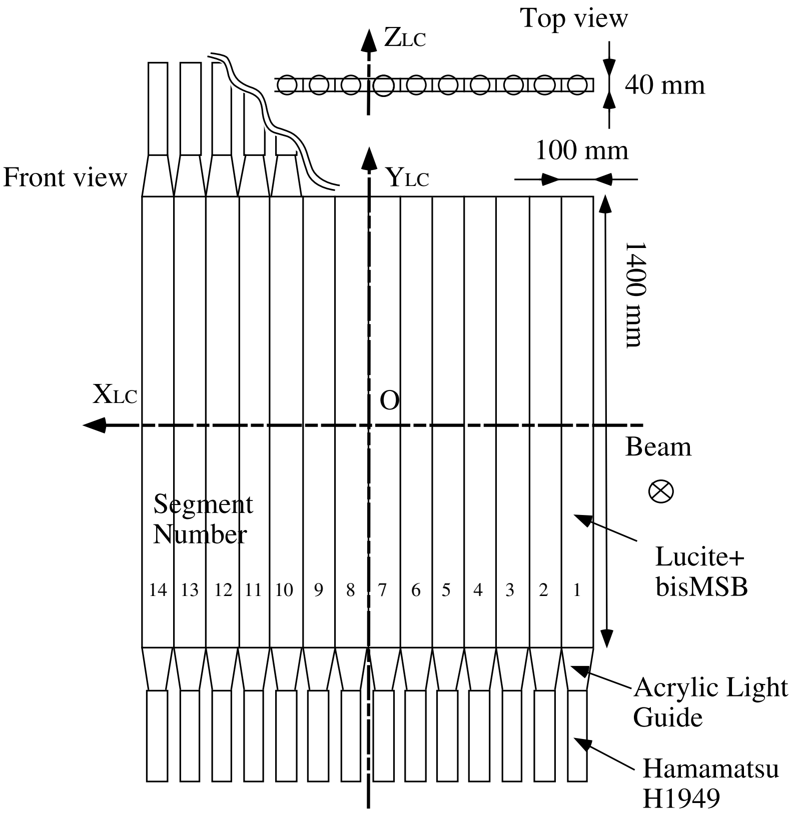

Figure 2.9: Schematic view of LC

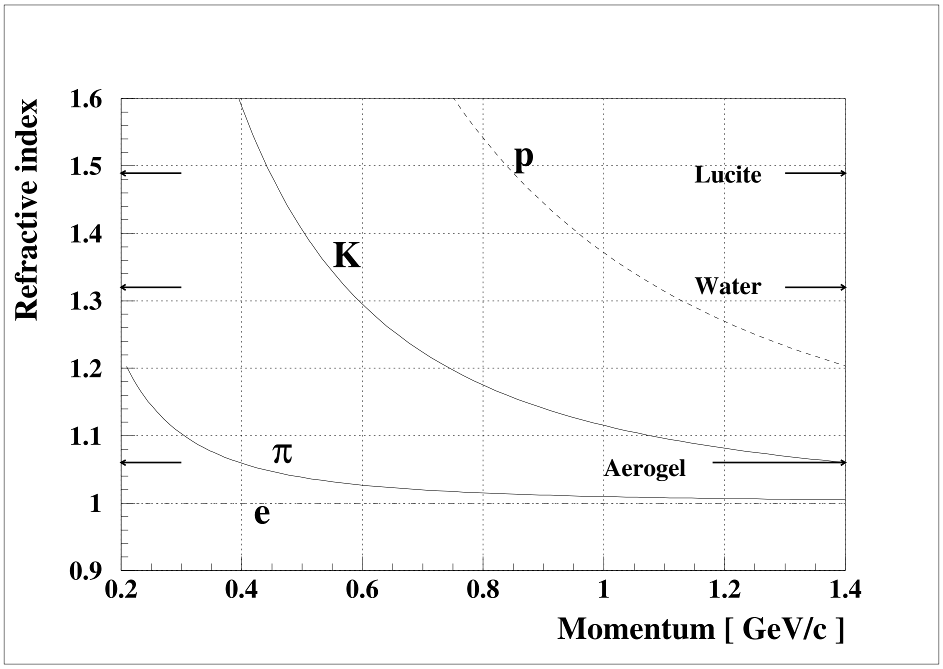

Figure 2.10: Threshold refractive index for Čerencov radiation as a function of momentum.

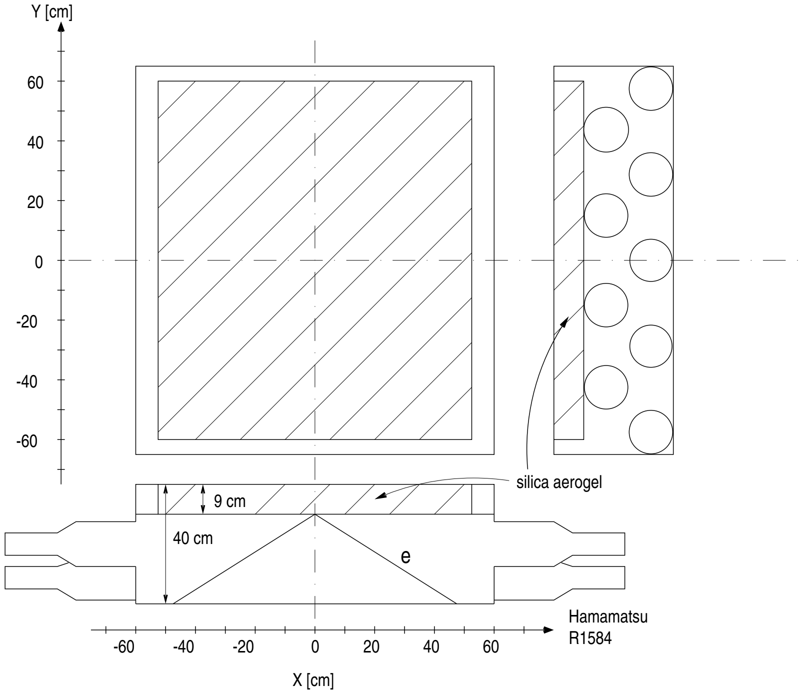

Figure 2.11: schematic view of AC.

Name	Area (cm)	Drift space (mm)	Wires	Thickness (in L_R)	Resolution (μm in r.m.s.)
BDC1-4	$24^W \times 15^H$	2.5	$xx'uu'vv'$	1.79×10^{-3}	300
SDC1	$40^W \times 15^H$	2.5	$xx'uu'vv'$	1.79×10^{-3}	300
SDC2	$56^W \times 15^H$	2.5	$xx'uu'$	1.18×10^{-3}	300
SDC3	$100^W \times 100^H$	21	$xx'yy'$	0.53×10^{-3}	250
SDC4X	$100^W \times 100^H$	21	$x \times 6$	1.05×10^{-3}	250
SDC4Y	$100^W \times 100^H$	21	$y \times 6$	1.05×10^{-3}	250

Table 2.4: Specification of the drift chambers.

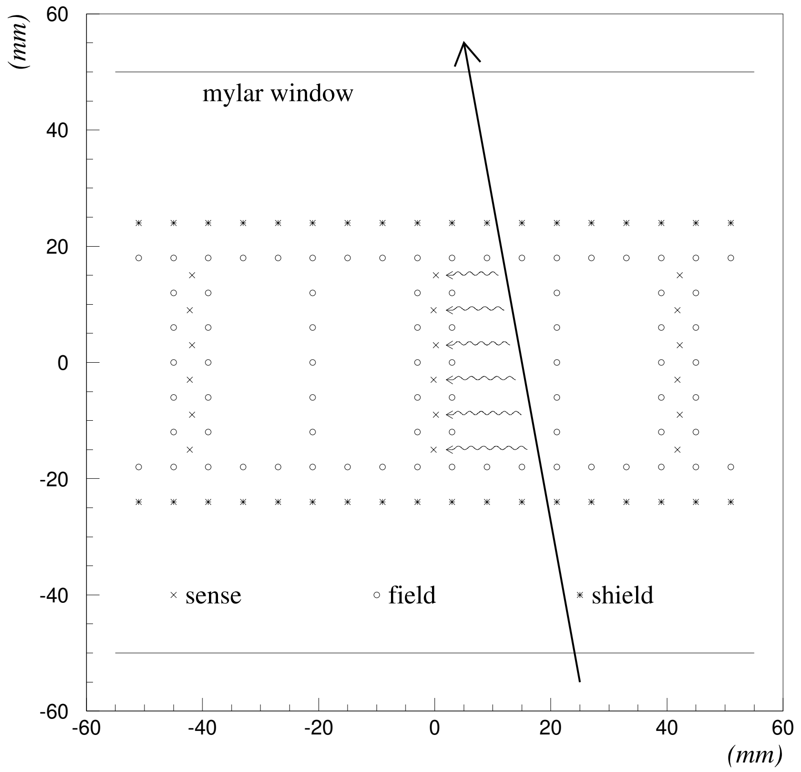

Figure 2.12: Cell structure of SDC4.

2.3 Decay counter

The decay counter was designed to measure energy and angle of both charged and neutral particles. The Top, Side and Bottom arms were installed to detect not only back-to-back events but also three or many body final states (Figure 2.13, decay-down, decaybird). Figure 2.16 shows the acceptance of coincident detection for the nucleon pair. Each decay arm was comprised of T2, T3 and Neutron counters(N). The Top and Bottom arms were equipped with drift chambers named PDC. T1 and T2(Figure 2.17,T2) were fast timing counters for incoming beam and outgoing decay particle, respectively. T1 had two layers named T11 and T12, and the second layer was used as BH2 in this experiment. The flight time between T11 and T12 can be used as reference quantity for the slewing correction of them(refer section 3.5). Specification of the decay counters are shown in Table 2.5.

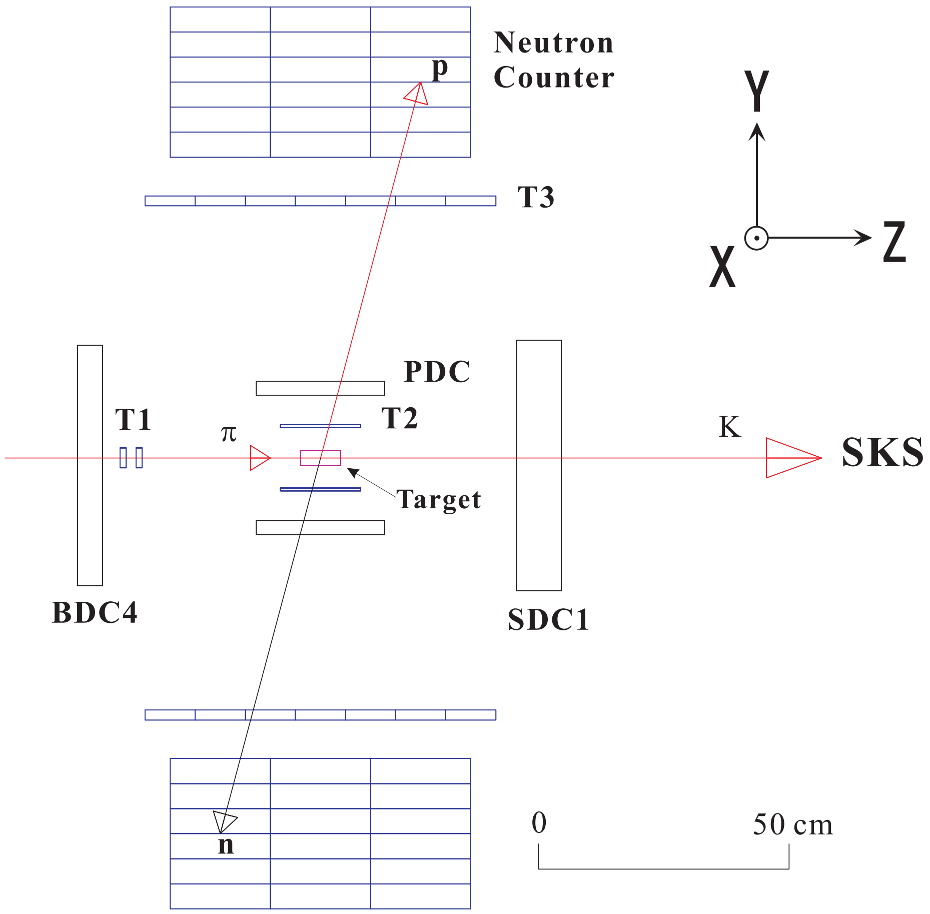

Figure 2.13: schematic view of decay counter seen along beam direction.

2.3.1 Charged particle detection

Charged particles were identified utilizing their dE/dx, total energy and flight time measured between T2 and T3. T2 served also as dE/dx counters. The sum of

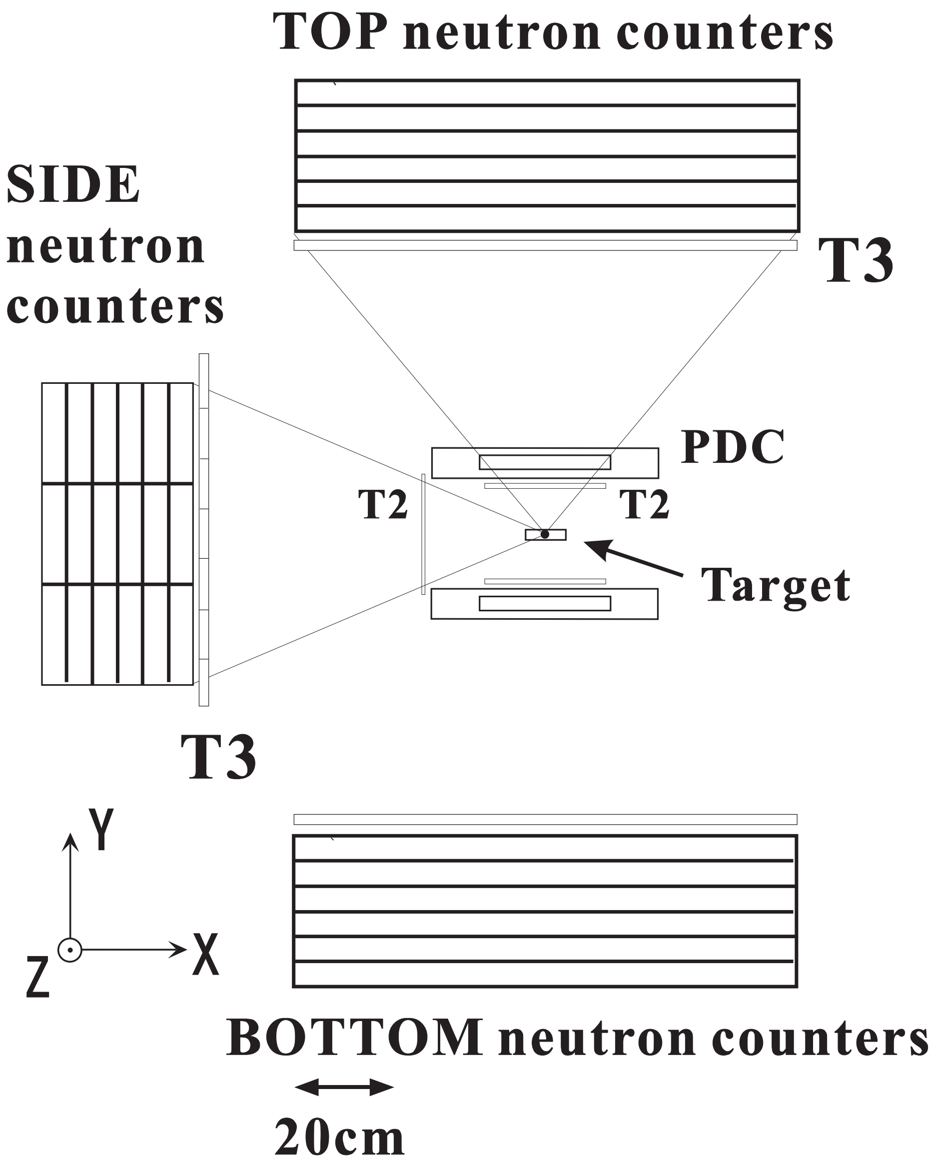

Figure 2.14: decay counter setup seen from beam downstream.

Name	Sensitive area (cm)	# of channel	Segmentation
T1	$9.8^{W} \times 4.0^{H} \times 1.2^{T}$	R3478S $\times$ 16	4-segments, 2-layer, 3-stage-booster
T2	$24.0^{W} \times 16.0^{H} \times 0.6^{T}$	R3478S $\times$ 12	6-segments
PDC	$26.0^{W} \times 26.0^{H} \times 2.8^{T}$	32 wires/plane	6-planes (xx', yy', xx')
T3	$100.0^{W} \times 70.0^{H} \times 2.0^{T}$	H1161 $\times$ 14	7-segments
Neutron	$100.0^{W} \times 60.0^{H} \times 30.0^{T}$	H1161 $\times$ 36	20 cm $\times$ 5 cm, 3×6 segments

Table 2.5: Specifications of the decay counters

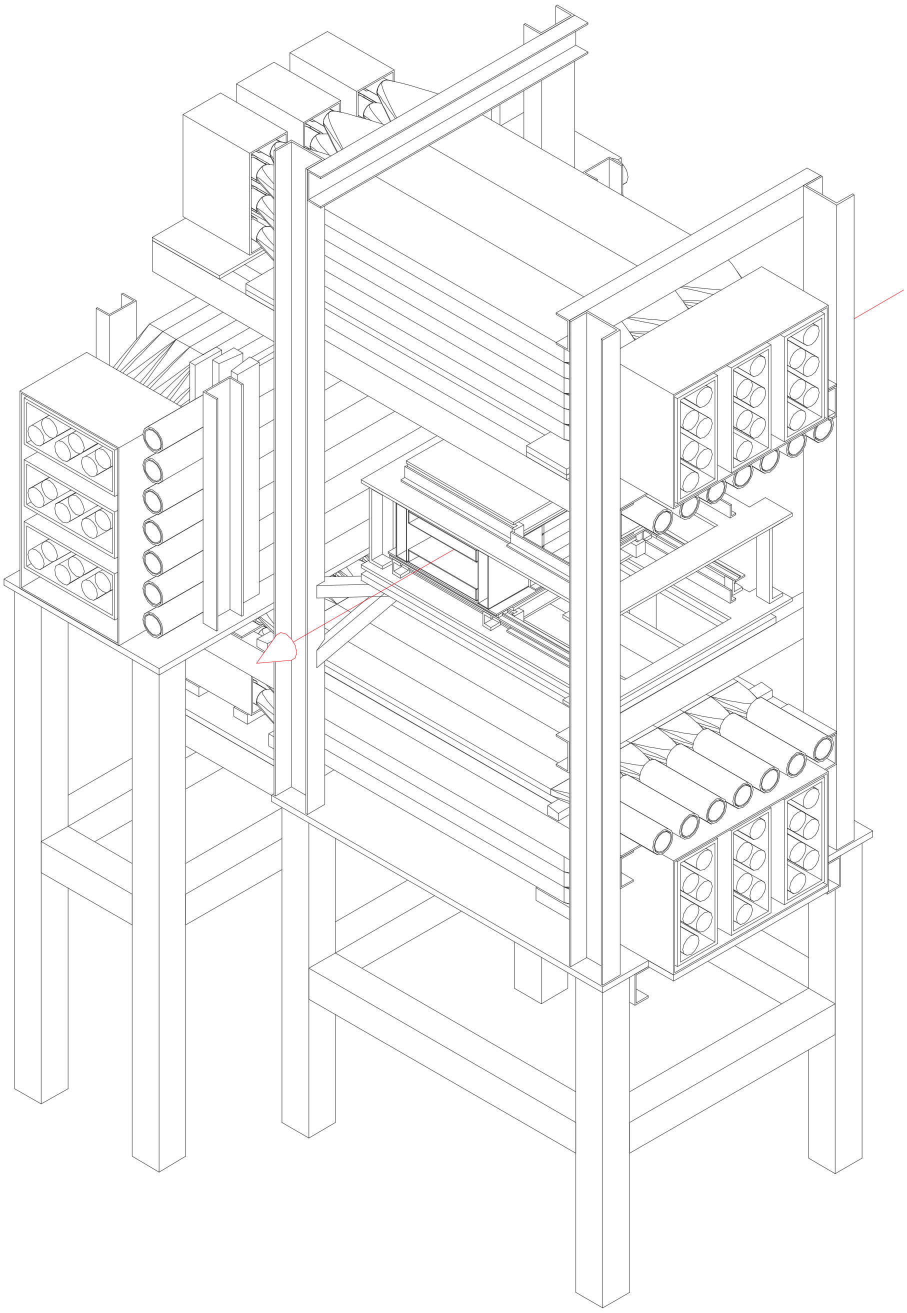

Figure 2.15: bird's eye view of decay counters. The arrow indicates beam direction.

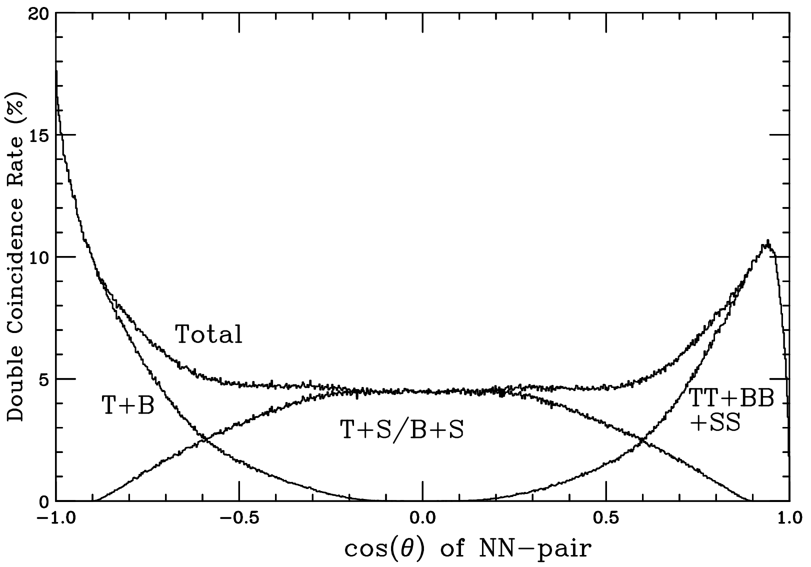

Figure 2.16: Double coincidence acceptance of decay counter for the nucleon pair as a function of the opening angle, where T,B and S denote Top, Bottom and Side arms, respectively.

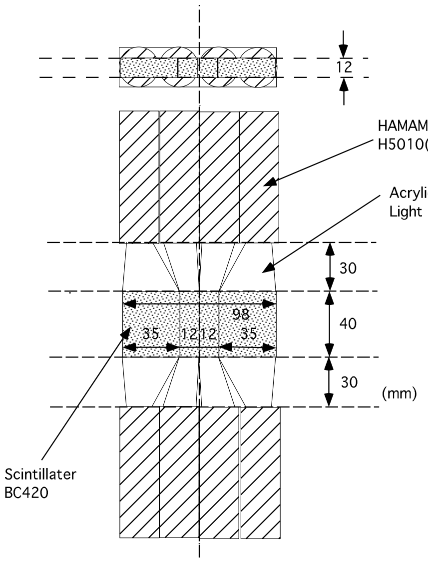

Figure 2.17: Schematic view of T1 counter. It is segmented to have equal counting rate.

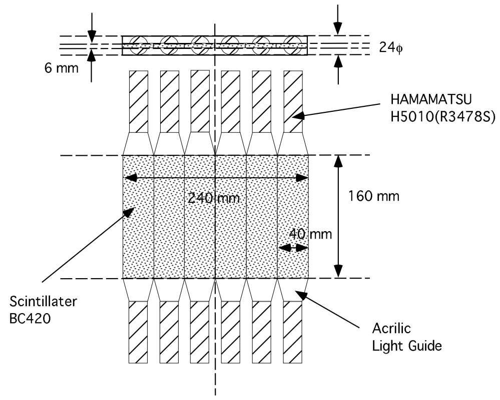

Figure 2.18: schematic view of T2 counter.

ADC data of the counters which charged particles passed through gave total energy information. PDC was used to analyze their trajectories.

2.3.2 Neutral particle detection

The Neutron counter(T4) had 6 layers to increase detection efficiency as much as possible. T3 counter was used to veto charged particles. The time difference of the PMTs attached on both ends of scintillators was used to obtain hit position in the Neutron counter. Neutron energy was derived from their flight from T1 to Neutron counters.

2.4 Trigger and data acquisition system

The online trigger was defined as Table 2.6. Several kinds of triggers were mixed for calibration purpose in addition to PIK trigger, which is the main trigger to collect (π^+, K^+) events. $PIPC(N)$ trigger was prepared to acquire $(\pi, pC(N))$ events, which means that a scattered proton was detected at the SKS and a charged(neutral) particle was detected at the decay counter. (π, pC) events were used to calibrate the time coordinate of the decay counters since (π, K) events are occurred by weak interaction and the decay particles are always emitted with delayed timing. The gate timing of the data taking system was re-defined by BH2(T1) counter after all the coincidence logic in order to hold the equality of data for all kinds of the triggers. $PIPI$ trigger intended to gather (π, π) events, which were suitable for calibration of SDC3 and 4 since beam pions are scattered with widespread angles. $BEAM$ trigger requires only BH1 and BH2 to have hits for checking the possible bias arising from other conditions. The γ emission events contained in $PIPN$ trigger were used for calibration of the Neutron counters.

Name	Definition	Prescale Factor	Trig./spill
$BEAM$	$BH1 \times BH2 \times \overline{GC}$	300×10^3	5
PIK	$BEAM \times TOF \times LC \times \overline{AC1} \times \overline{AC2}$	1	150
$PIPI$	$BEAM \times TOF \times LC$	3×10^3	12
$PIPC$	$BEAM \times TOF \times \overline{AC1} \times \overline{AC2} \times \sum_i T2_i \times \sum_i T3_i$	17	50
$PIPN$	$BEAM \times TOF \times \overline{AC1} \times \overline{AC2} \times \sum_i (\overline{T3_i} \times N_i)$	11	50

Table 2.6: Online trigger definition. The subscript i means Top, Side and Bottom arm of decay counter.

Figure 2.19 depicts trigger logics for $BEAM$, PIK and $PIPC$. All the counters except for GC and AC were equipped with two PMTs attached on the both ends, and mean timer modules(MT) were used to remove incident position dependence of trigger timing. Pulse height and timing information of the signals were digitized by ADC and TDC modules of TKO standard, and stored into the buffer of the VME-MP(memory partner) event by event. They were processed by the host computer

HP743rt and written on the DVD-RAM disks once a beam-repetition cycle. The data were independently processed and monitored on the Linux-PC.

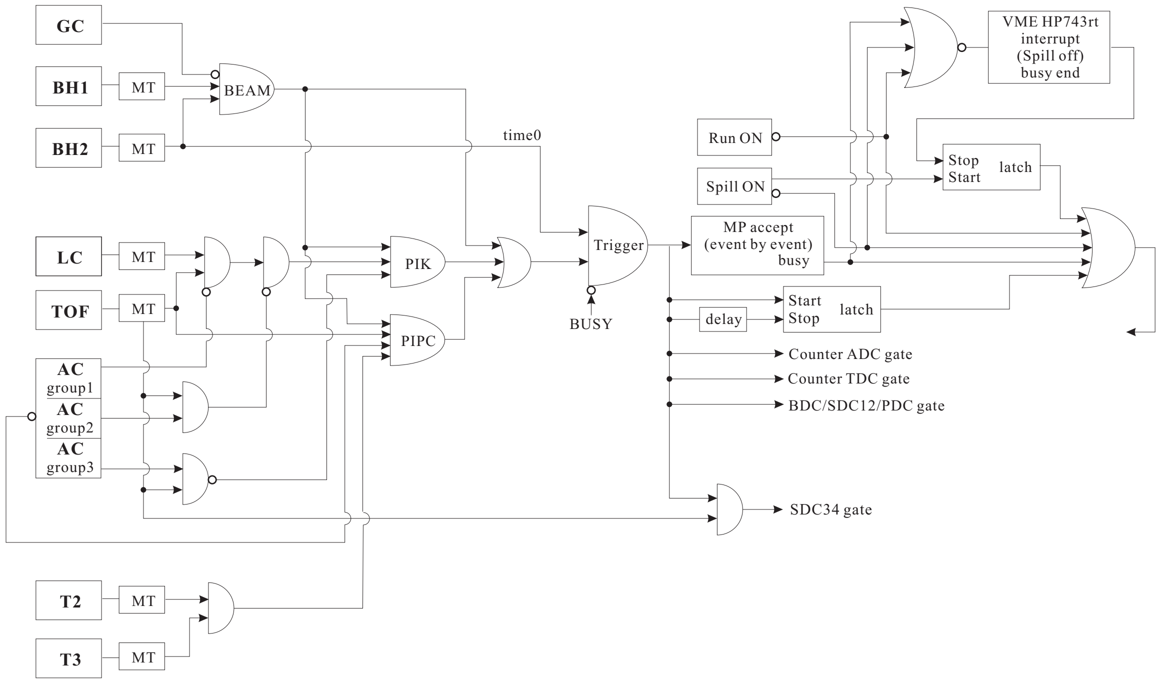

Figure 2.19: Trigger logic diagram. MT denotes mean timer module.

2.5 Experimental target

^{6}Li target had 50 mm width, 25 mm height and 80 mm thickness. It was wrapped with aluminized film to avoid oxidation.

2.6 Data summary

In year 2000 and 2001, 7.56×10^{11} and 1.63×10^{12} counts of pion were used for the experiment. In this thesis, accumulated data in the first year were analyzed.

Chapter 3

Analysis

3.1 Identification of hypernuclear formation

3.1.1 Background rejection

Figure 3.1 shows flight time spectrum between BH1 and BH2. Kaon contamination was separated as delayed component, which were enhanced in PIK trigger. The main peak was accepted as pions. This was examined for all combinations of the fired segments. Particle trajectories behind the SKS were roughly estimated by connecting each fired segment of TOF wall and LC, and it was checked whether they passed the sensitive area of SDC3 or not.

3.1.2 Beam spectrometer analysis

At first, the straight tracks were defined locally at BDC12 and BDC34. Hit positions on each planes were decoded from the drift time data and hit pattern of pair planes. They were linearly fitted by the least-square method and combinations of the points which gave less chi-square than a cut-off value were saved in buffer as the candidates.

Next, the tracks at the entrance and exit of QQDQQ were connected to minimize the chi-square defined by:

$$\chi^2_{QQDQQ} \equiv \frac{1}{n-5}\left\{\sum_{i=1}^{12} H_i \left(\frac{P_i - f_i(\vec{X}_{in})}{w_i}\right)^2 + \sum_{i=13}^{24} H_i \left(\frac{P_i - g_i(\vec{X}_{out})}{w_i}\right)^2\right\} \tag{3.1}$$

$$n = \sum_{i=1}^{24} H_i \tag{3.2}$$

$$H_i = \begin{cases} 1 & \text{if } i\text{th plane has a hit.} \\ 0 & \text{if } i\text{th plane has no hit.} \end{cases} \tag{3.3}$$

$$\vec{X}_{out} = \mathcal{M}(\vec{X}_{in}, \delta) \tag{3.4}$$

where P_i and w_i is the hit position and weight of ith plane. $\vec{X}_{in}$ and $\vec{X}_{out}$ stand for vectors of the trajectory at the entrance and the exit of the QQDQQ. $f_i(\vec{X}_{in})$ and $g_i(\vec{X}_{out})$ are hit position of ith planes for the trajectory. $\vec{X}_{out}$ was calculated by the transport matrix($\mathcal{M}$), which is a function of relative momentum($\delta = p/p_0$). The matrix was calculated by *ORBIT*[31]. Figure 3.2 and Figure 3.3 show typical distribution of χ^2_{QQDQQ} and beam momentum, respectively.

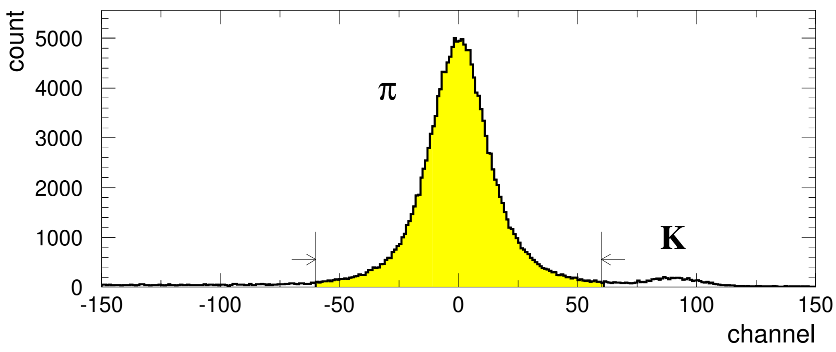

Figure 3.1: Flight time spectrum between BH1 and BH2. The delayed component represents kaon mixed in beam. The arrows indicate the region accepted as pion.

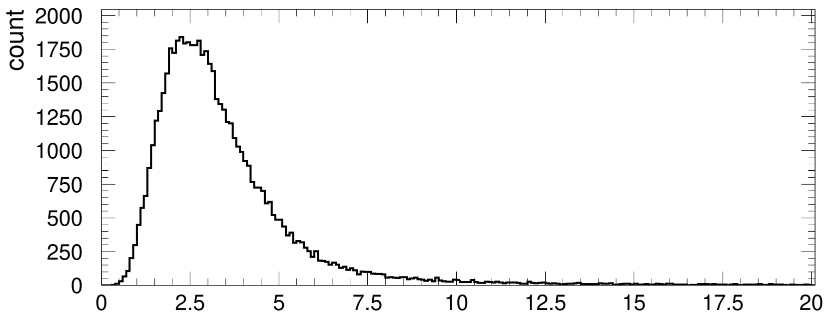

Figure 3.2: Typical distribution of χ^2_{QQDQQ}.

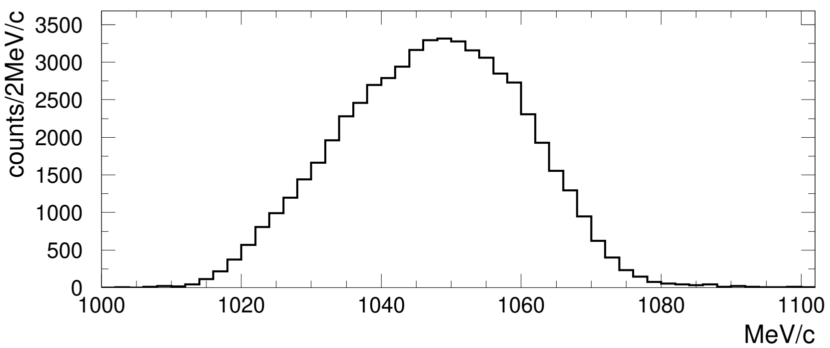

Figure 3.3: Typical beam momentum distribution.

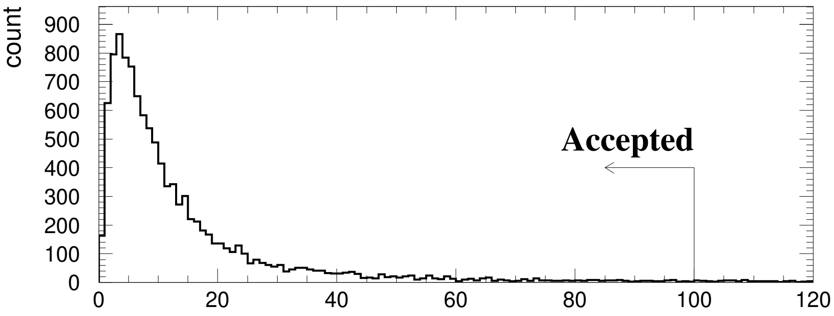

Figure 3.4: Typical χ^2_{SKS} distribution. Cut condition is indicated by the arrow.

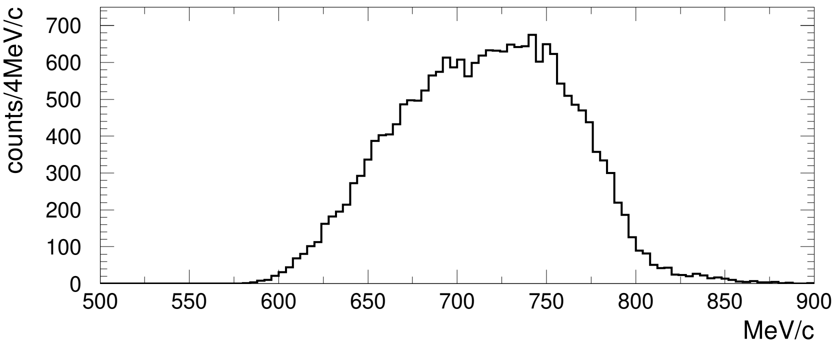

Figure 3.5: Typical momentum distribution of scattered particle.

3.1.3 SKS analysis

At first, linear fitting was tried inside each of SDC12 and SDC34 in similar way to BDCs. First and sixth wire of SDC4 were not used since the electric field was not very uniform there. At least three of other planes were required to have hits.

Next, the track passing through the SKS was determined to minimize chi-square(χ_{SKS}) which has five parameters to be optimized, momentum, two independent positions and two independent angle at the target:

$$\chi^2_{SKS} = \frac{1}{n-5}\sum_{i=1}^{n}\left(\frac{x_i^{tracking} - x_i^{data}}{w_i}\right)^2 , \tag{3.5}$$

where $x_i^{tracking}$, x_i^{data} and w_i are hit position of tracking, data and weight on ith planes, respectively. Figure 3.4 and Figure 3.5 show typical distribution of χ_{SKS} and the momentum of scattered particles for (PI, K) data.

3.1.4 Event selection

The reaction point was determined as the center of closest approaches of beam track and SKS track. The events which originate from reaction with target material were selected as shown in Figure 3.6.

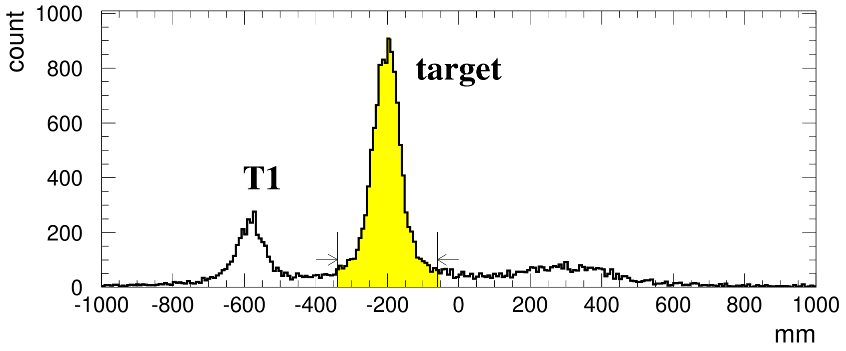

Figure 3.6: Typical distribution of Z-vertex. The arrows indicate the events selected as the target region.

Figure 3.7 shows mass spectra of scattered particles for PIK trigger(top) and $PIPC$ trigger(bottom) given by following equation:

$$m = \frac{p\sqrt{1-\beta^2}}{\beta} , \tag{3.6}$$

where p is the momentum obtained by SKS analysis, and β is the velocity derived from the flight time between BH2 and TOF wall. kaons were clearly separated from pion and proton. (π, pX) events contained in PIK trigger and $PIPC$ trigger were also identified to calibrate time coordinate of the decay counter. In case that BH2 or TOF wall has multiple hits, all the combinations were examined and one of the fired BH2 which gave the mass closest to that of real kaon was adopted.

Finally, hypernuclear mass (M_{HY}) was calculated by the kinematical relation for the (π, K) reaction:

$$M_{HY} = \sqrt{(E_\pi + M_A - E_K)^2 + (p_\pi^2 + p_K^2 - 2p_\pi p_K \cos\theta)} , \tag{3.7}$$

where M_A is the target nuclear mass, θ is the scattering angle, E_π, E_K, p_π and p_K are the energy and momentum of pion and kaon. Figure 3.8 is $M_{HY} - M_A$ spectrum for PIK trigger, which means the difference of the missing mass and ^{6}Li mass. The ground state of $^6_\Lambda$Li was observed as the peak around 180 MeV/c^2.

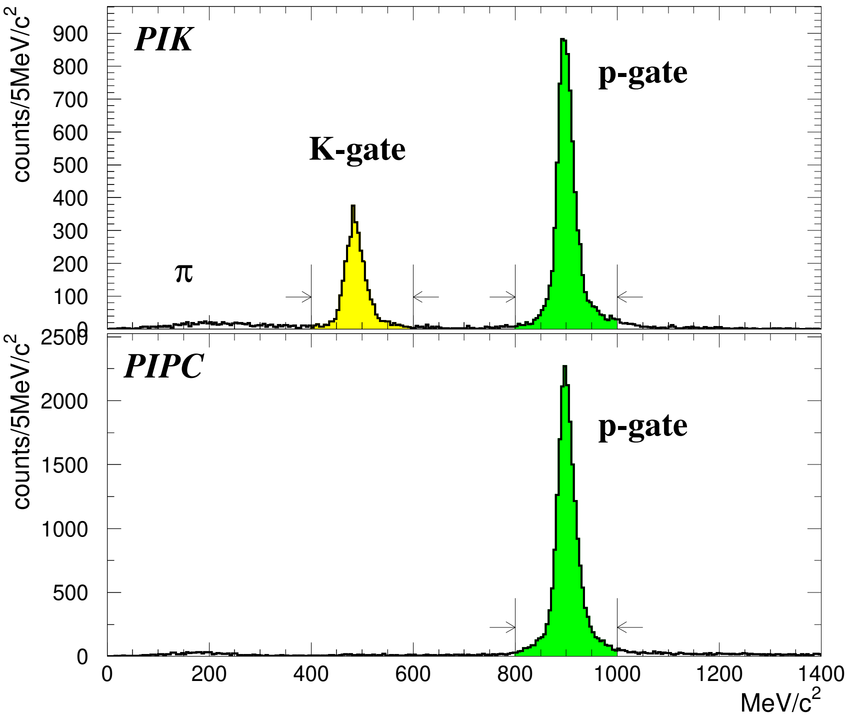

Figure 3.7: Typical mass distribution of scattered particles for PIK trigger(top) and $PIPC$ trigger(bottom). The arrows indicate accepted region.

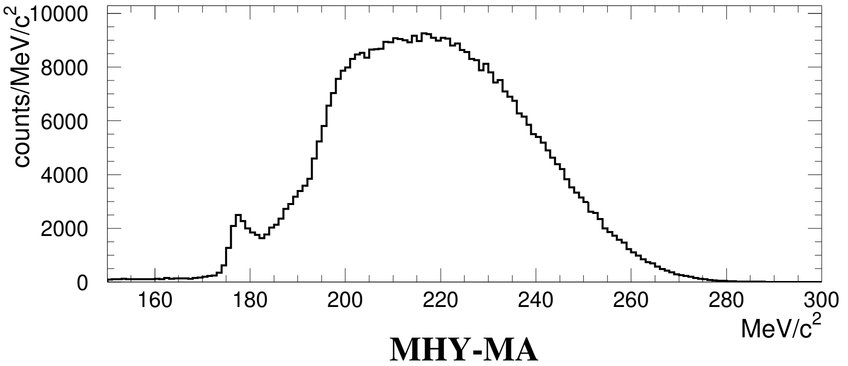

Figure 3.8: Observed excitation spectrum of $^{6}\mathrm{Li}(\pi^+, K^+)^{6}_{\Lambda}\mathrm{Li}$ reaction.

3.2 Charged particle identification

Charged particles detected at the decay counters were identified by means of the correlations between dE/dx and total energy, time of flight(TOF) and total energy. dE/dx means energy loss per unit length, and ADC data of T2 were referred as dE/dx. TOF was measured between T2 and T3. The ADC sum of sequentially fired counters was approximately regarded as proportional to the total energy. Two kinds of PID function were defined as:

$$PID \equiv \frac{y_{data} - y_{\pi}(E)}{y_p(E) - y_{\pi}(E)} \tag{3.8}$$

$$y = \begin{cases} dE/dx & (PID1) \\ TOF & (PID2) \end{cases} \tag{3.9}$$

y_p and y_π were $dE/dx(PID1)$ or $TOF(PID2)$ as a function of total energy(E) for proton and pion. They were obtained by fitting the proton line and pion line in the scatter plot of dE/dx and E, or TOF and E with polynomial function:

$$y = P_1 + P_2/E + P_3E + P_4E^2 \tag{3.10}$$

(see Figure 3.2). y_{data} is the data point. PID1, PID2 and their scatter plot are exhibited in Figure 3.10. Two ways of the particle identification gave a sufficient π-p separation as shown Figure 3.10(bottom).

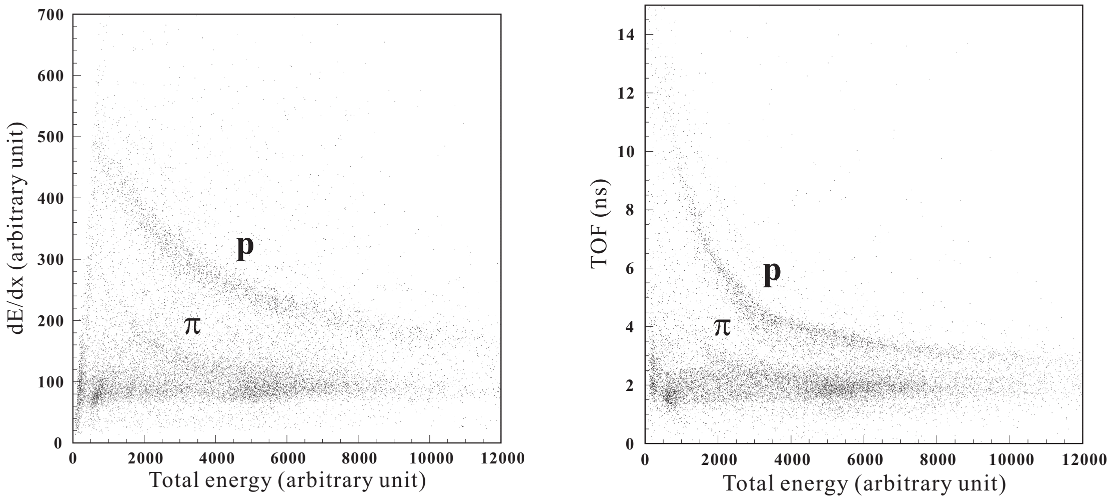

Figure 3.9: Scatter plot of TOF and total energy(left), and dE/dx and total energy(right) for $PIPC$ events.

Figure 3.11 shows missing mass spectra of (π^+, K^+) reaction with coincident pion or proton. Ground state of ${}^{6}_{\Lambda}$Li is clearly separated from quasi-free Λ enough to evaluate the number in both inclusive and coincident spectra. The signal to background(over bound region) ratio is as good as 9 for inclusive spectrum. In proton-coincident spectrum, ground state and the peak around 200 MeV are much enhanced. It indicates that detected protons mainly originate from non-mesonic decay of ${}^{5}_{\Lambda}$He, which $s_n^{-1}s_\Lambda$ and $p_n^{-1}s_\Lambda$ states of ${}^{6}_{\Lambda}$Li decay into(refer Figure 1.7). The cut point is determined to select the ground state of ${}^{6}_{\Lambda}$Li to exclusively study the decay of ${}^{5}_{\Lambda}$He.

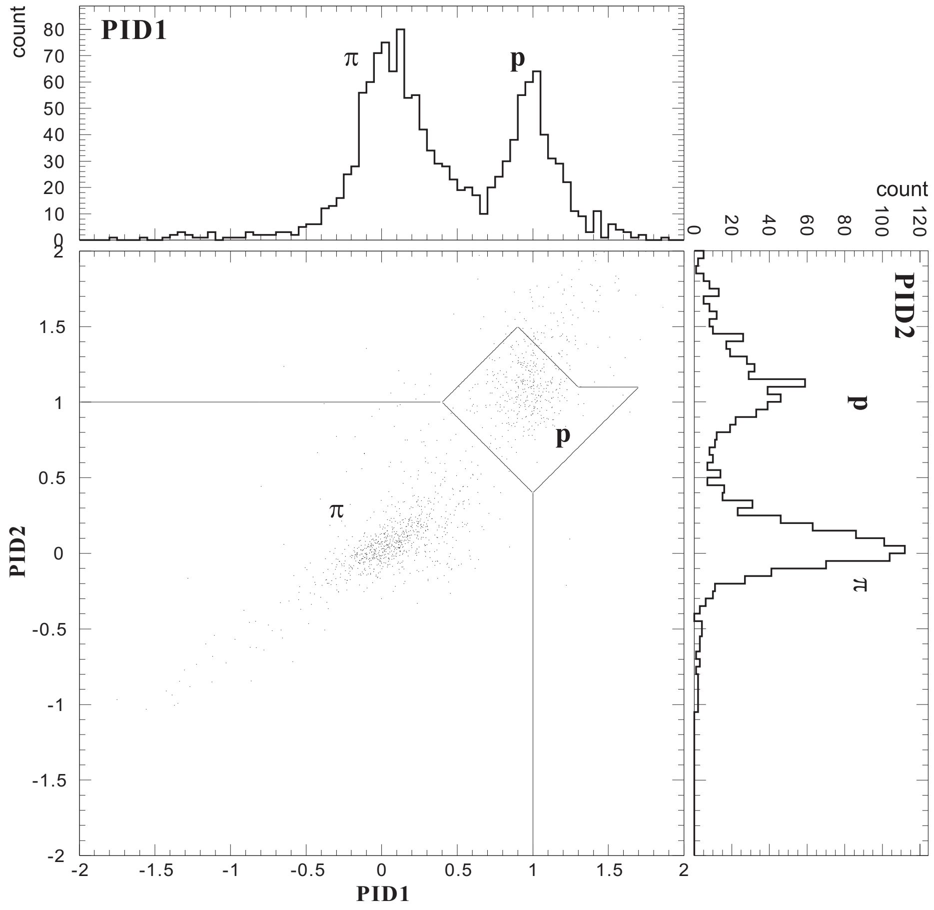

Figure 3.10: Two kinds of PID function and their 2-dimensional plot for (π, K) event gated at the ground state of ${}^{6}_{\Lambda}$Li. The lines indicate the criteria for proton-pion separation.

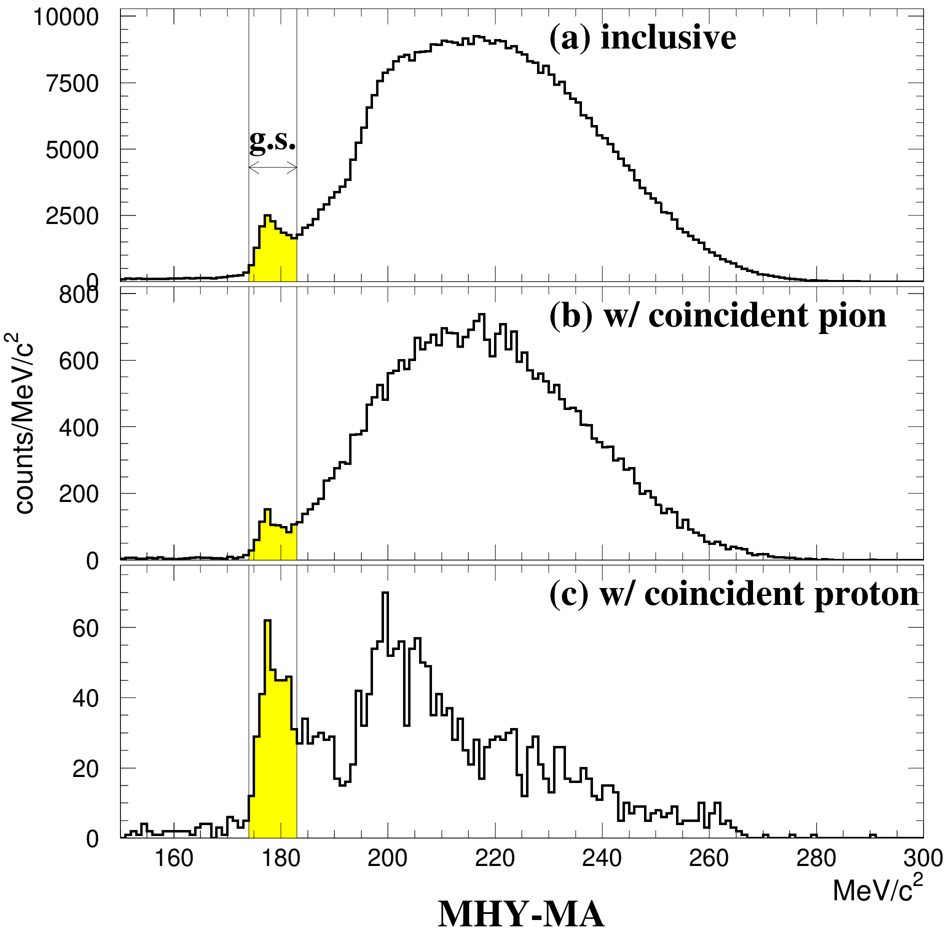

Figure 3.11: Missing mass(MHY-MA) spectra for (π^+, K^+). The events in 174 MeV$\leq$ MHY $-$ MA $\leq$183 MeV are identified as the ground state of ${}^{6}_{\Lambda}$Li, which decay into the ground state of ${}^{5}_{\Lambda}$He.

3.3 PDC analysis

PDC had large drift cells compared to BDC and SDC12, thus hit positions on each planes were extracted from the table converting drift time to drift length. It was calibrated so that perpendicularly injecting particles reproduce uniformly distributed drift length. Figure 3.12 shows the structure of PDC, where y and z axis correspond to vertical direction and beam direction. z-component of the track was obtained by fitting hit positions on four x-planes. The decay particle trajectories tend to be so tilted that both left and right candidates were examined. The vertex was derived as the point of intersection between the tracks of beam and the decay particle. Figure 3.13 shows obtained vertex image. Figure 3.16 compares Z-vertex for (π, pX), $(\pi, K\pi)$ and (π, Kp) events, where X means a charged particle detected at the decay counter. It shows much better horizontal position resolution than that solved by beam pion and scattered kaon(Figure3.6), and well reproduced the target thickness(8 mm). Tail on the downstream in $(\pi, K\pi)$ events represents the decay of free Λ formed in quasi-free production. Considering that recoiled hypernuclei stops in much shorter period than their lifetime, cut point was determined to select target region.

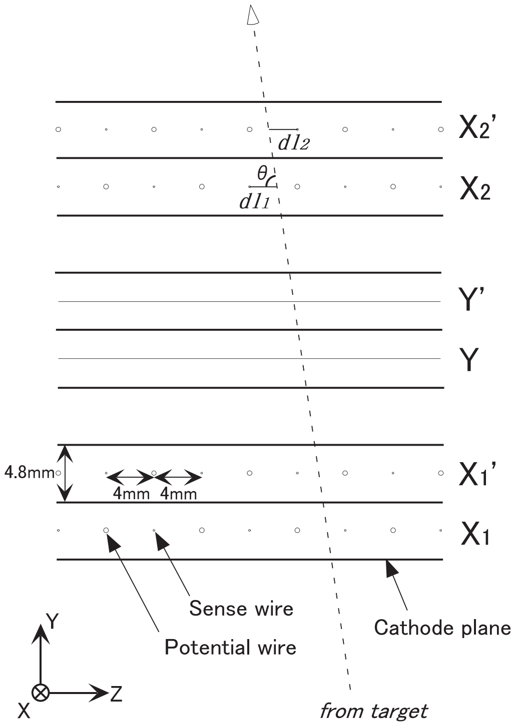

Figure 3.12: Structure of PDC.

x-component of the track was obtained by fitting hit positions on two y-planes and the vertex. For multiple hit, all candidates were examined and best track was accepted under the criterion that chi-square was less than 100. Figure 3.14 shows typical chi-square distribution of linear fitting for z direction and x direction. Typical resolution of PDC was shown in Figure 3.15.

3.4 Range analysis

Energy measurement of charged particle by the TOF method between T2 and T3 had a difficulty in calibrating the velocity, due to lack of favorable events for the purpose such as cosmic ray. Therefore another approach utilizing ADC data was developed for year 2000 data. It is noted that following procedure can be applied only to proton, since a stopped pion generates secondary particle through their decay or absorption by the nucleon, and the range and ADC information are not very reliable for pion.

It is known that light output of the scintillators tends to be saturated as dE/dx

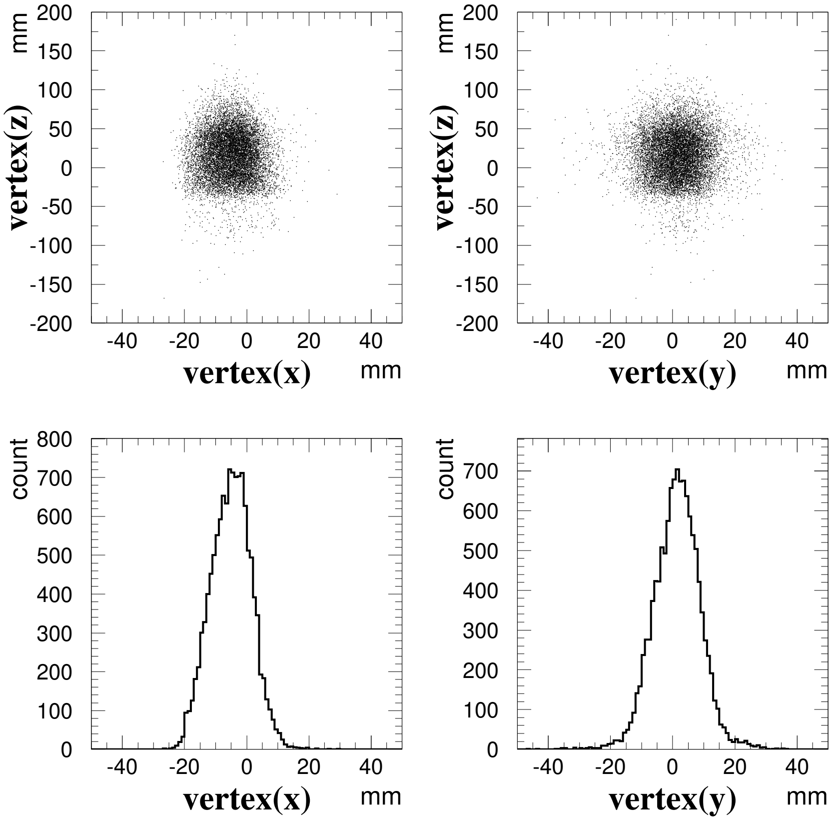

Figure 3.13: Vertex image solved by PDC and BDC34 tracking.

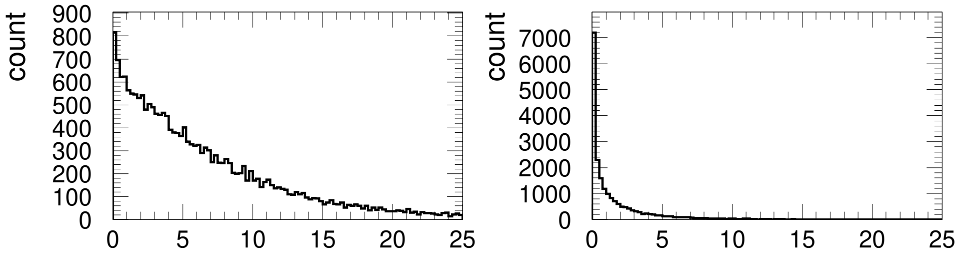

Figure 3.14: Typical distribution of reduced chi-square for Z-Y fitting (left) and X-Y fitting(right) of PDC.

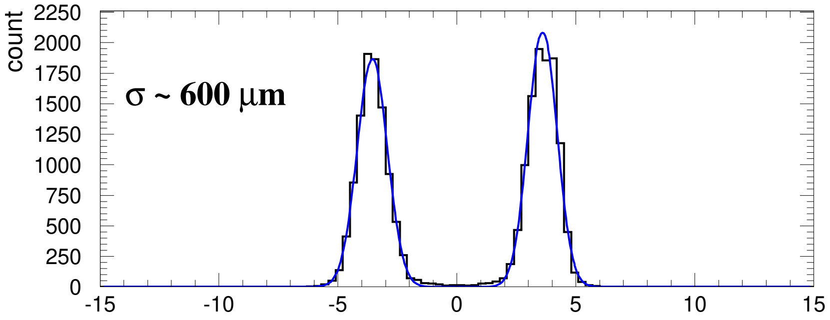

Figure 3.15: Typical resolution of PDC. It is defined as $dl1 - dl2 \pm 4.8 \times \tan\theta$, where dl1 and dl2 are drift length of the pair plane, and $\tan\theta$ is a slope of the tracking vector (see Figure 3.12).

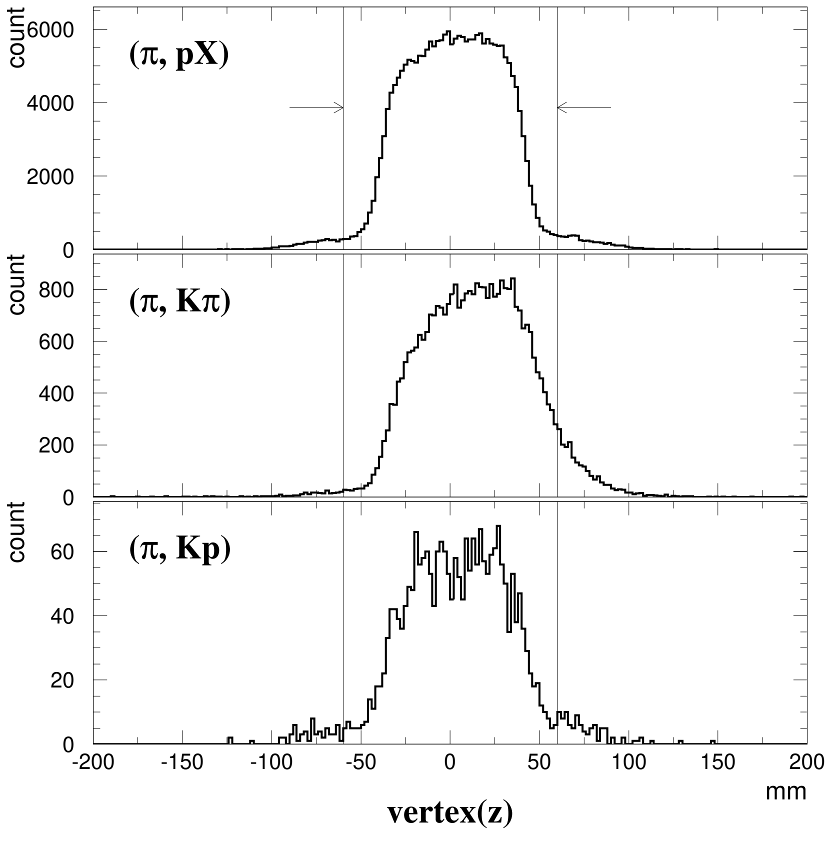

Figure 3.16: Z-vertex distribution for(π, pX), $(\pi, K\pi)$ and (π, Kp) events. The target region surrounded with the lines was accepted.

becomes larger. Birks proposed to fit the relation by following function[29]:

$$\frac{dL}{dx} = \frac{A\frac{dE}{dx}}{1 + kB\frac{dE}{dx}} , \tag{3.11}$$

where dL/dx and dE/dx denote the light output and energy deposit of the charged particle per unit length, respectively. A is a factor which depends on gain of the counter, and the saturation effect is included by a factor kB.

In the present analysis, parameters A and kB were determined by following method.

First, ADC data of all counters were calibrated using minimum ionizing particles. Parameter A was defined by:

$$A = q/\Delta E_{av.} , \tag{3.12}$$

where q is mean ADC and $\Delta E_{av.}$ is the averaged energy deposit in the counter for the pions which stopped at the fifth layer of the Neutron counter. The saturation effect was assumed to be negligible for them. $\Delta E_{av.}$ was estimated using simulation code LEPS[30], considering the tracking angle. A was independently defined for T3 and the Neutron counter. The proton which travels the longest path to stop inside the scintillator leaves maximum energy. Therefore the highest end of the ADC spectrum corresponds to such events, and the edge becames clearer by selecting perpendicular injection. dE/dx of such proton was calculated by LEPS for every 0.1 mm travel, and kB is determined to reproduce the data point by Birk's formula (3.11). Obtained kB was 0.10 mm/MeV and consistent with the old data:0.13 $\pm$ 0.02 mm/MeV[29].

Once A and kB are fixed, the penetration depth can be derived as a funtion of ADC data of the stopping counter. Figure 3.17 shows typical distribution of ADC data(middle) and calculated penetration depth(bottom) of first layer of the Neutron counter, and scatter plot between ADC data of that counter and T3(top) for protons whose tracking angles were larger than 0.95 in cosine. The edge represents 5 cm-range protons, whose kinetic energy was about 80 MeV according to LEPS.

Total range of the particle(R) was expressed as follows:

$$R = \left(\sum_{i=1}^{N-1} T_i \right) / \cos\theta + d , \tag{3.13}$$

where N and T_i denote the number of sequentially fired counters and each thickness. $\cos\theta$ is the tracking angle and d is the penetration depth. Finally, kinetic energy was obtained from R using LEPS.

However for a few counters, the highest edge of ADC was considerably smaller than that of the others, although the degree of the saturation is characteristic of the material. The gain of PMTs were set low enough to cover a wide range of the energy, and its poor linearity might be responsible for the discrepancy. The parameter A was re-defined for such abnormal counters. Figure 3.18 shows the proton energy spectra gated at the ground state of ${}^{6}_{\Lambda}$Li. The top figure gives the kinetic energy out of the experimental target, while energy loss in the target was considered in the bottom figure. The kinetic energy at the production point was derived from "corrected" range:

$$R_{cor} = R + l_{target} \times (D_{target}/D_{ps}) , \tag{3.14}$$

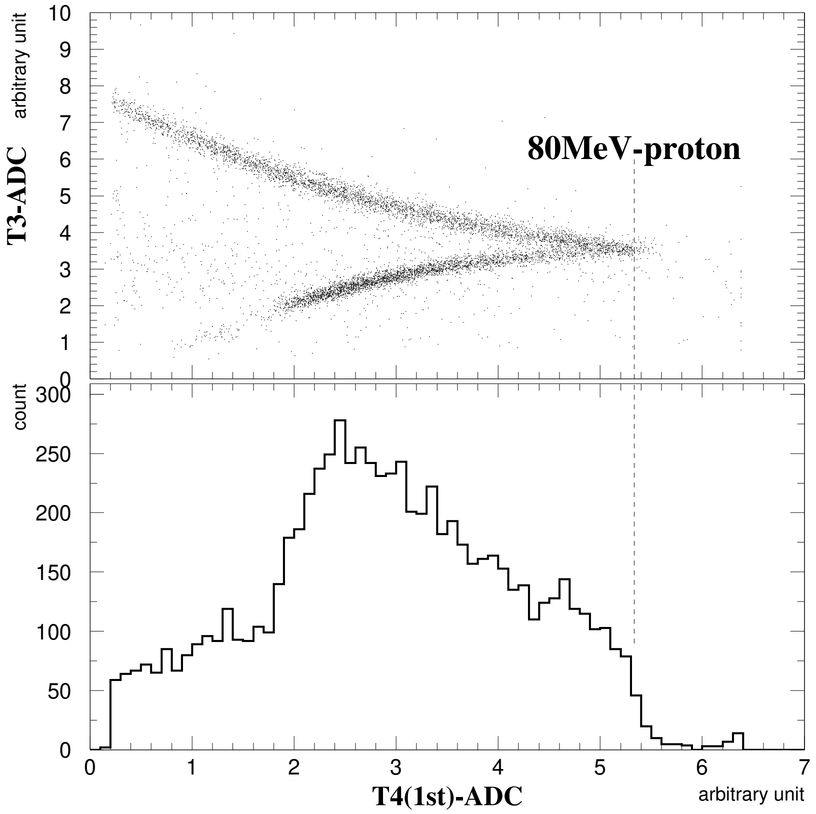

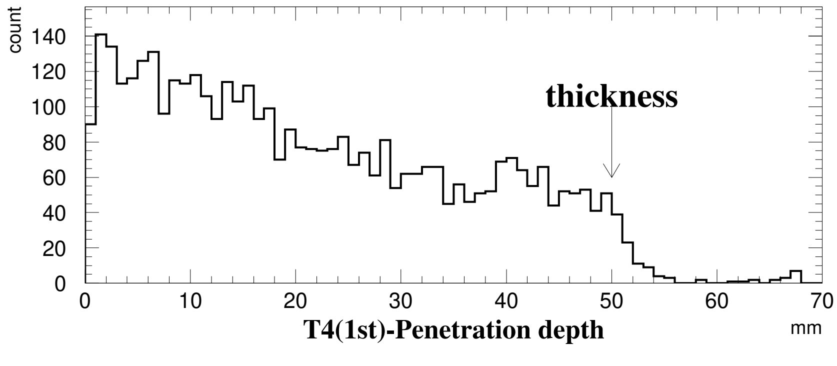

Figure 3.17: ADC data(middle) and penetration depth(bottom) of first layer of the Neutron counter, and its correlation to ADC data of T3(top) selecting perpendicular incoming protons($\cos\theta \geq 0.95$). The highest end of ADC data corresponds to 80 MeV according to LEPS.

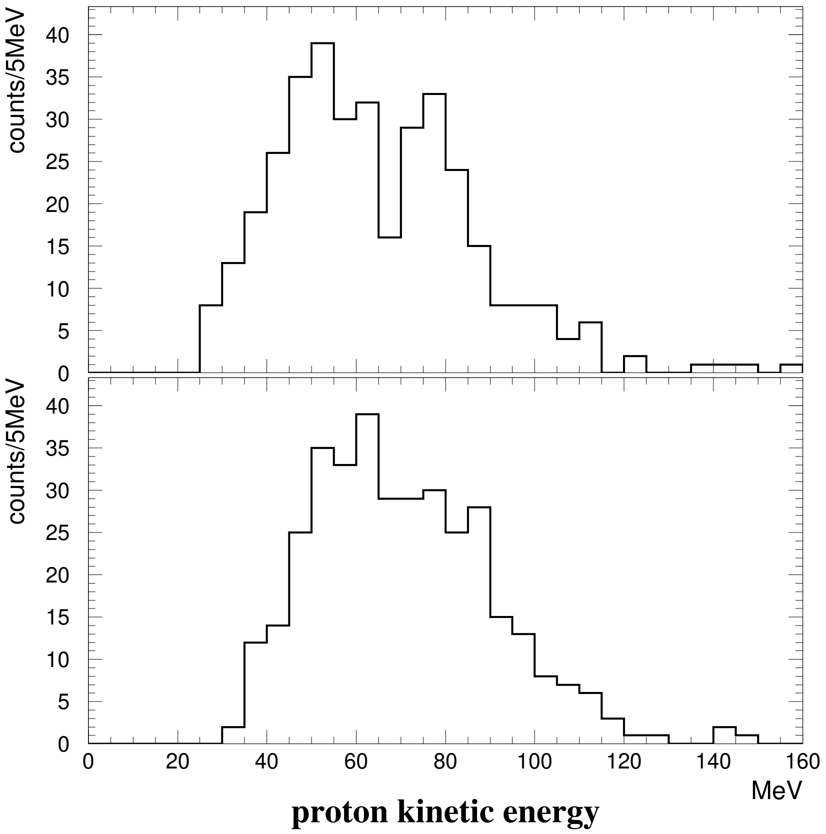

Figure 3.18: Proton energy spectra gated at the ground state of ${}^{6}_{\Lambda}$Li. Top figure correspond to proton energy out of the target, while naive correction was applied to the bottom figure to compensate for the energy loss in the target.

where l_{target} means the path length inside the target, D_{ps} and D_{target} mean density of the plastic scintillator and target, respectively. Considering that both T2 and T3 were required to have hits for the particle identification, the appropriate threshold was supposed to be 42 MeV,

3.5 Lifetime analysis

3.5.1 Basic concept

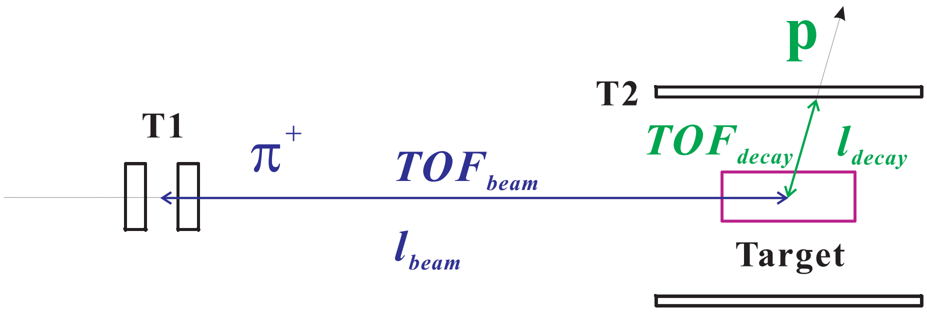

The decay time of hypernuclei(Δt) is obtained by subtracting its production time (i.e. beam injection time) from the charged particle emission time. It is derived by following equation:

$$\Delta t = t_{T2} - TOF_{decay} - TOF_{beam} - t_{T1} \ , \tag{3.15}$$

$$TOF_{decay} = \frac{l_{decay}}{\beta_{decay} c} \ , \tag{3.16}$$

$$TOF_{beam} = \frac{l_{beam}}{c} \ , \tag{3.17}$$

where t_{T2} and t_{T1} denote the time when beam pion hits T1 and decay particle hits T2, respectively. TOF_{decay} and TOF_{beam} mean the flight time of the beam from T1 to the target and the flight time of the decay particles from the target to T2, respectively. They were obtained as their flight path(l_{beam}, l_{decay}) divided by their velocities(c, $\beta_{decay}c$), where c represents light velocity. Proton was used as decay particle for the present analysis, whose velocity was extracted from the kinetic energy analyzed in previous section. Mean time of T11 and T12 was used as t_{T1}, expecting that the accuracy would be $1/\sqrt{2}$ times improved by taking an average of two equivalent and independent data.

The decay time Δt obeys the probability density function:

$$P(t) = \frac{1}{\tau} \exp\left(\frac{t}{\tau}\right) \ , \tag{3.18}$$

where τ is the lifetime of the hypernucleus. In real measurement, it fluctuated due to a finite timing resolution of the detectors. The measured Δt distribution can be expressed as the convolution of $P(t)$ by $R(t)$:

$$P'(t) = \int_{-\infty}^{t} P(t-u)R(u)du \tag{3.19}$$

$$= \frac{1}{\tau}\int_{-\infty}^{t} \exp\left(\frac{t-u}{\tau}\right) R(u)du \ . \tag{3.20}$$

$R(t)$ represents the time response function of the system, which was obtained as the decay time for prompt (π, pp) events. The time coordinate was calibrated to adjust mean of prompt time distribution to be 0 for all the combination of T1 and T2. (π, pp) events acquired by $PIPC$ trigger were utilized in addition to that contained in PIK trigger so as to follow the fluctuation of TDC data for every run with sufficient statistics(see Figure 3.19).

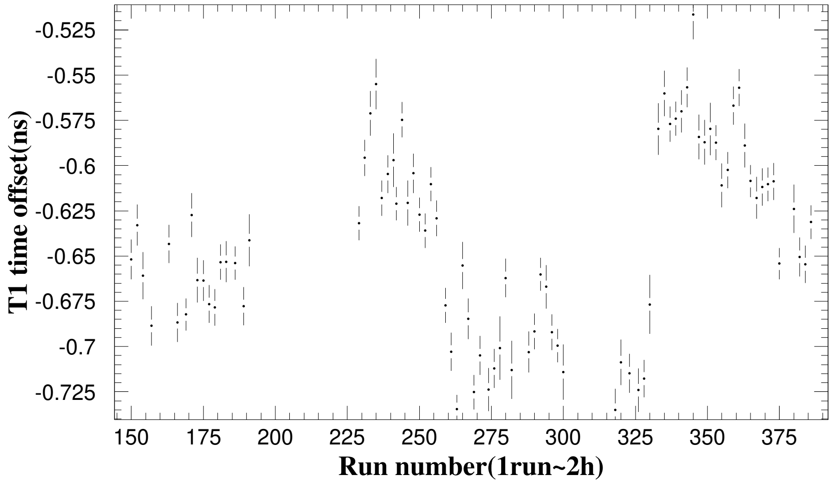

Figure 3.19: Typical run dependence of T1 time offset (1run $\sim$ 2h.).

Figure 3.20 compares the prompt time spectra constructed using (π^+, pp) reaction collected by PIK trigger(top) and $PIPC$ trigger(bottom). It was confirmed that both kinds of the triggers gave equal timing information.

As shown in Figure 3.21, no correlation was observed between prompt time and proton velocity, which demonstrates the validity of the proton energy spectra(Figure 3.18).

3.5.2 Beam event selection

Under a high rate beam, multiple pions sometimes generate piled up pulse and make the timing resolution worse. Such events can be seen as the secondary peak in ADC spectrum. Figure 3.22 is the scatter plot of ADCs of T11 and T12. The lines shows accepted region.

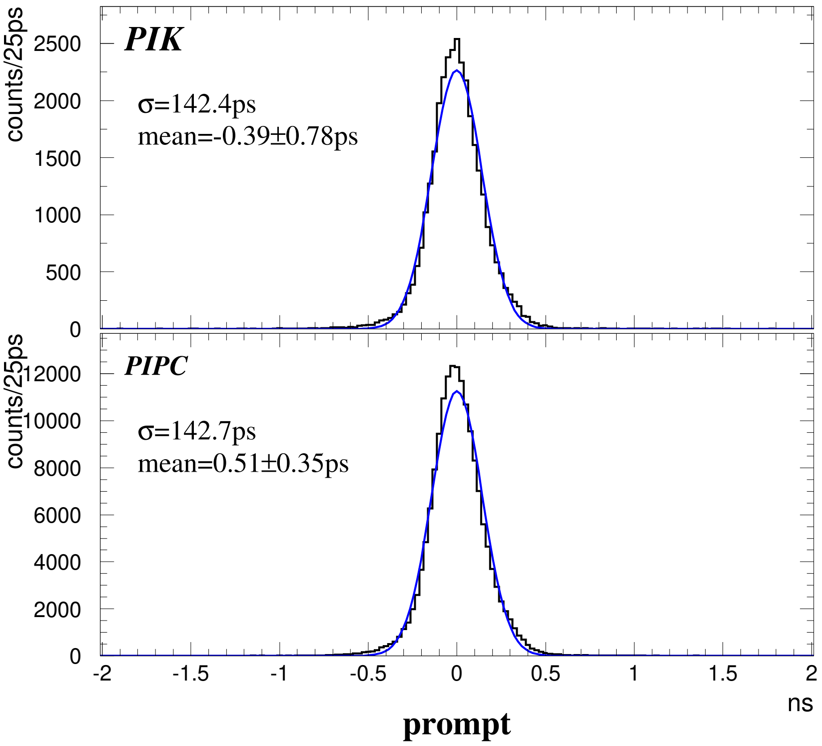

Figure 3.20: Prompt time spectra for PIK trigger(top) and $PIPC$ trigger.

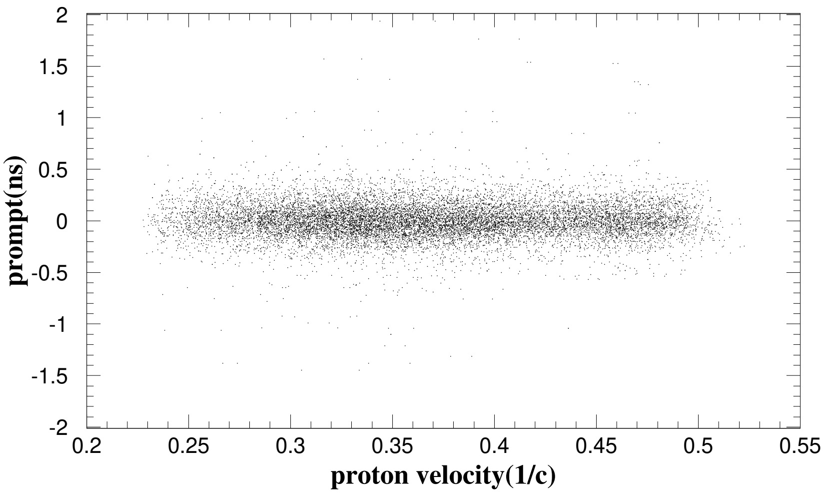

Figure 3.21: Scatter plot of the proton velocity and prompt time.

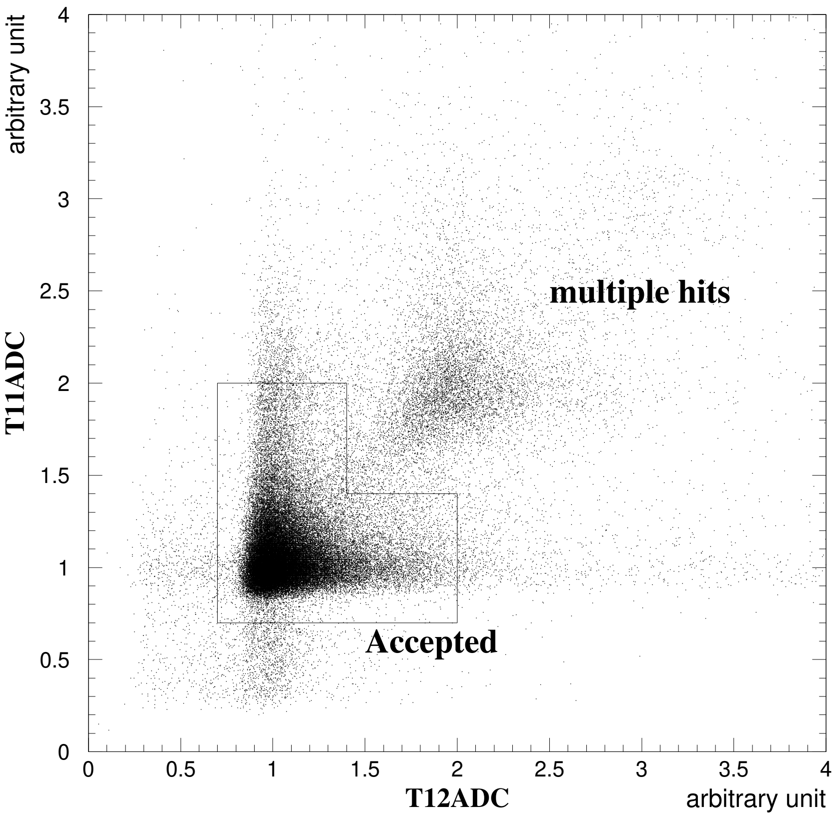

Figure 3.22: The scatter plot of ADC data of T1 first layer(T11) and second layer(T12). The secondary peak which arise from multiple hit were rejected.

3.5.3 Slewing correction for T1 and T2

In general, the timing of discriminator output depends on the pulse height of the input signal, and thus this effect should be corrected in order to obtain sufficient time resolution(slewing correction)[28]. The TDC data of T11, T12 and T2 were corrected according to following expression:

$$t_{true} = t_{observed} - \left\{ W_1 \left(\frac{1}{\sqrt{q}} - \frac{1}{\sqrt{q_0}} \right) + W_2 \left(\frac{1}{\sqrt{q}} - \frac{1}{\sqrt{q_0}} \right)^2 \right\} , \tag{3.21}$$

where q and q_0 mean ADC data and the most probable ADC data as a reference point, respectively. The coefficients W_1 and W_2 were determined to remove the pulse height dependence of the TOF which can be assumed to be constant. For T11 and T12, beam flight time($t_{T11}-t_{T12}$) between them were used(Figure 3.23). As shown in Figure 3.23, standard deviation of $t_{T11} - t_{T12}$ distribution was improved to be 81 ps for the best pair with slewing correction. The intrinsic resolution of T1 counters were evaluated to be 60 ps in sigma, assuming T11 and T12 have equal timing resolution.

In case of T2, prompt time was directly corrected(Figure 3.24).

3.5.4 Y-vertex correction

As shown is Figure 3.25(right), considerable correlation between prompt time and vertical position of the vertex was observed especially for the Top arm. Though the source of this correlation was not studied yet, the phenomenological correction can applied as shown in Figure 3.25(left). The systematic error due to this correction should be carefully checked in the future.

3.5.5 Fitting method

Lifetime was derived by fitting obtained decay time distribution by maximum likelihood method as follows:

1. Define two histograms filled with prompt time data and decay time data respectively. Size of each bins were determined as 25 ps.

2. Calculate probable entry of each bin of decay time spectrum according to the probability density function defined as the convolution of exponential distribution and observed time response function with a lifetime value as a parameter.

3. Calculate the log-likelihood function defined by:

$$\mathcal{F} \equiv \sum_i \left[f_i - N_i - N_i \log \frac{f_i}{N_i} \right] , \tag{3.22}$$

   where f_i and N_i denote estimated and observed event number of ith bin.

4. Iterate 2-3 over the range of parameter from 50 to 400 ps.

5. The lifetime parameter which gave best fit was adopted. The error was defined as the value which varied the likelihood function $\pm 1/2$.

Figure 3.26 shows prompt time spectrum(top) and decay time spectrum gated at the ground state of ${}^{6}_{\Lambda}$Li(bottom). Obtained lifetime was 282^{+21}_{-19} ps.

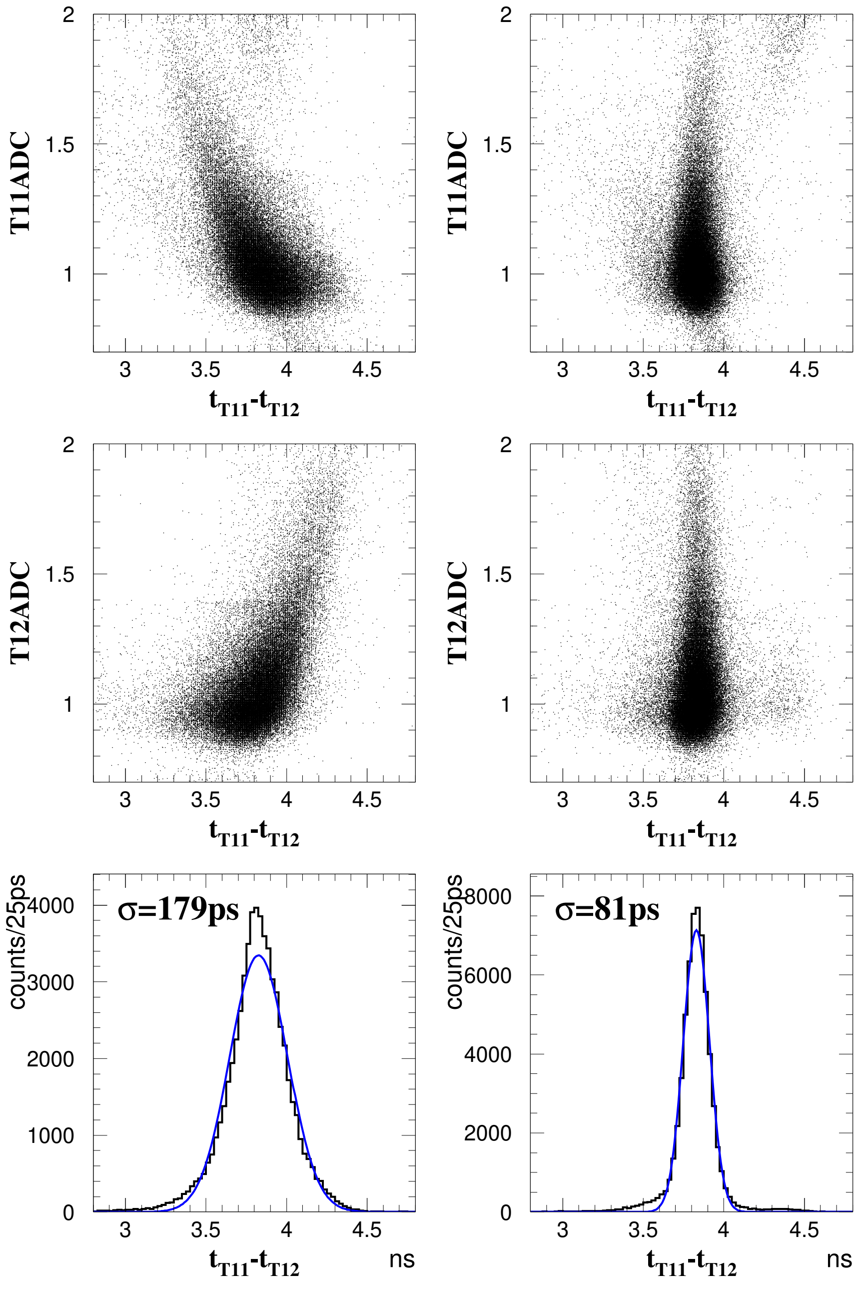

Figure 3.23: Time difference between T11 and T12 $(t_{\mathrm{T11}} - t_{\mathrm{T12}})$(bottom) and its dependence to ADC data of T11(top) and T12(middle) without slewing correction(left) and with slewing correction(right). The intrinsic time resolution of T1 was evaluated to be $\sigma = 60$ ps for the best pair.

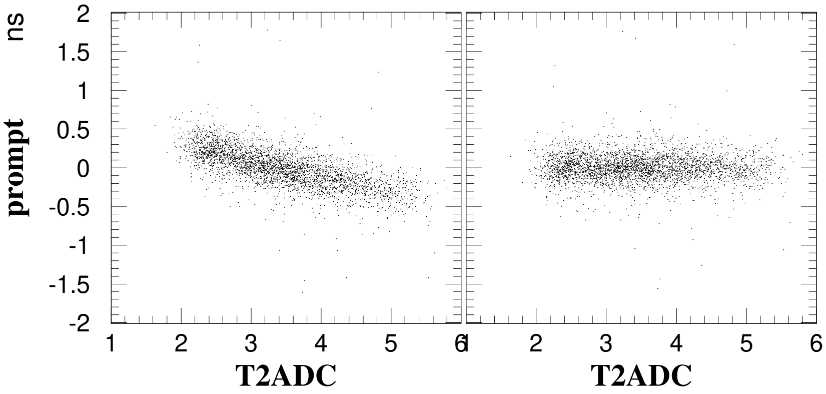

Figure 3.24: Scatter plot of T2ADC and prompt time without correction(left) and with correction(right).

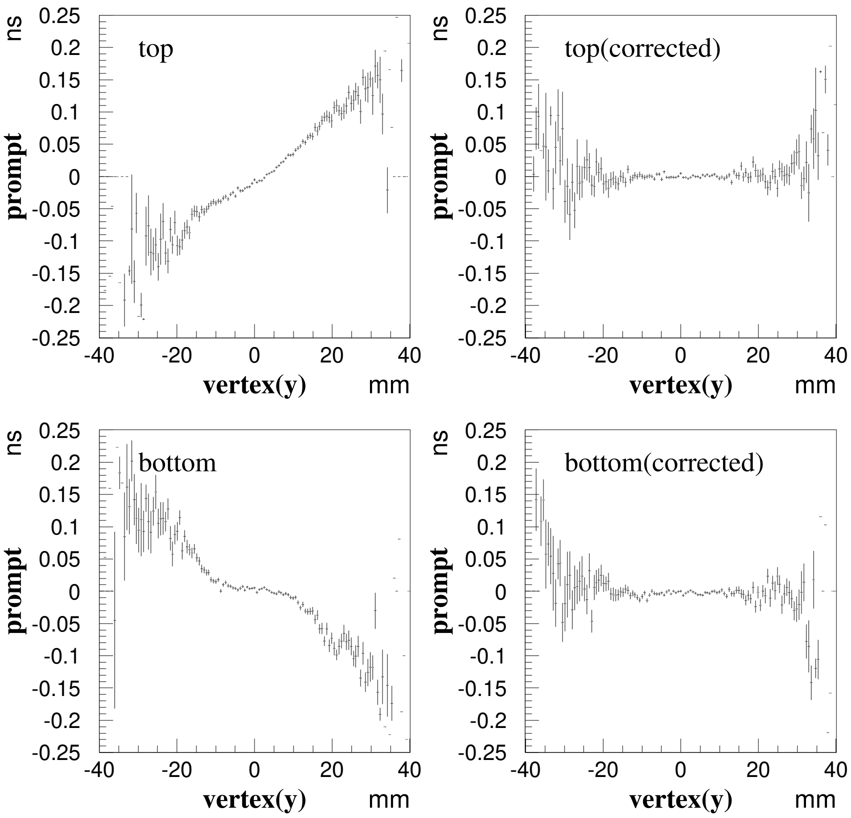

Figure 3.25: Scatter plot of mean of prompt time and Y-vertex with correction(left) and without correction(right).

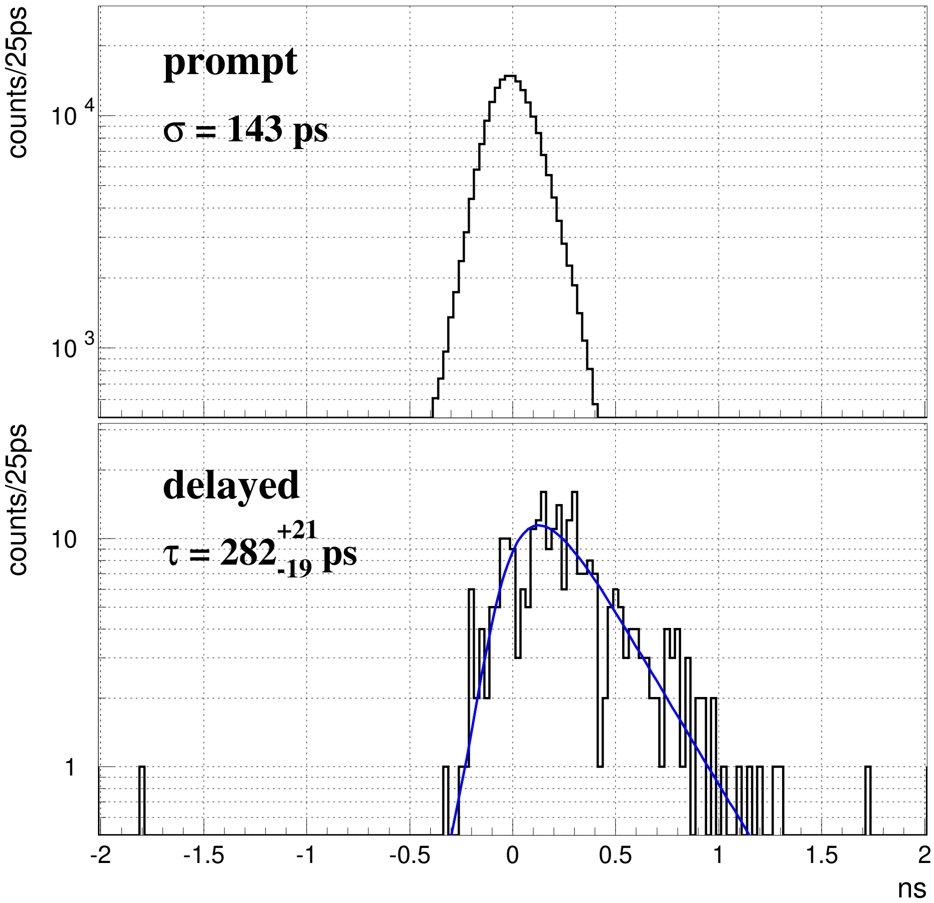

Figure 3.26: prompt time spectrum(top) and decay time spectrum(bottom) gated at the ground state of ${}^{6}_{\Lambda}$Li.

Chapter 4

Results and discussion

4.1 Lifetime

The lifetime of ${}^{5}_{\Lambda}$He was preliminary determined as 282^{+21}_{-19} ps in the present analysis. Compared with the previous measurement(256 ± 20 ps), a little longer lifetime was shown with slightly better error level(7%). The difference is not very significant now(about 1.3 σ), but the accuracy better than 5% will be accomplished by adding the data of year 2001.

Assuming the lifetime is τ, resolution of the time response function is σ_{res} and the available event number was N counts, the error of the lifetime measurement σ_{τ} can be approximately written as:

$$\sigma_{\tau} \sim \sqrt{\frac{\tau^2 + \sigma_{res}^2}{N}} \ . \tag{4.1}$$

Hence the accuracy is improved in proportion to the square root of the statistics.

The number of available proton will reach 3.2 times the one of year 2000 even if neglecting qualitative improvement of the new data. The second experiment was performed under lower beam rate, which was preferable in several respects. T1 was relieved from serious multiple hits, which had to be discarded in the offline analysis. The tracking efficiencies of BDC and SDC are also expected to be improved. Owing to sufficiently accumulated cosmic-ray data, gain tuning and slewing correction of decay counters will be much easier and reliable.

Present analysis method also has room to be improved. The tracking efficiency of PDC was as low as 70%, which can be still improved, since the present analysis requires all the planes to have hits although that is too strict in case the efficiency is more important rather than the position resolution.

Partial decay width Γ_{π^-} is derived from the equation:

$$\Gamma_{\pi^-} \equiv b_{\pi^-}\Gamma_{tot} \ , \tag{4.2}$$

$$b_{\pi^-} = \frac{N_{\pi^-}}{\varepsilon_{\pi^-}\Omega_{\pi^-}N} \ , \tag{4.3}$$

$$\Gamma_{tot} \equiv 1/\tau \ , \tag{4.4}$$

where N_{π^-} is the number of detected π^-, ε_{π^-} and Ω_{π^-} is the detection efficiency and the acceptance of decay counter for π^-, respectively. As shown in Figure 3.11, hypernuclear formation was successfully identified in (π, K), $(\pi, K\pi)$ and (π, Kp) events. Further analysis will be proceeded to determine the π^- branching ratio b_{π^-} within 5% error, and Γ_{π^-} within 10% error for the purpose of distinguishing Isle potential and SG potential with 1σ level.

4.2 Proton spectrum

The obtained proton energy spectrum(Figure 3.18) from ${}^{5}_{\Lambda}$He seems similar to both the theoretical prediction and the previous experimental results [4][5] as far as its shape above the threshold. For precise comparison, Monte Carlo simulation is required based on the actual experimental setup.

On the other hand, the preliminary result neutron energy spectrum shows no peak structure, similarly to that of E369. It is interesting to examine the energy and angular correlation between the proton and neutron to derive the proton-stimulated non-mesonic decay rate.

Chapter 5

Summary

${}^{5}_{\Lambda}$He hypernucleus was produced by ^{6}Li$(\pi^{+}, K)^{6}_{\Lambda}$Li reaction and its decay products(proton and pion) were identified by the decay counter. Preliminary analysis using about 30% of whole data gave proton energy specrum from non-mesonic decay and lifetime(282^{+21}_{-19}) of ${}^{5}_{\Lambda}$He with a few times higher statistic than previous experiment. More refined results will be given by adding the rest of data. It is one of our goal to drive partial decay width of ${}^{5}_{\Lambda}$He and provide the conclusive information to probe the feature of Λ-nucleus potential.

Acknowledgement

I would like to express my gratitude to Prof. O. Hashimoto. He gave me the opportunity to participate this experiment and encouraged me many times.

I am very grateful to Prof. S. N. Nakamura. He patiently read my draft and gave me valuable advices to complete this thesis.

I would like to express my sincere gratitude to Mr. H. Outa, who is a spokesperson of KEK-PS E462 experiment. This work was owed to his precious advice and support throughout the preparation, experiment, and analysis. I was much enlightened by his profound knowledge of physics and experiment.

I am deeply grateful to Dr .Y. Sato. He achieved a great work in KEK-PS E307, and I learned many things about analysis method from him.

I would like to thank Prof. H. Bhang, Prof. T. Nagae, Dr. S. Ajimura and Dr. H. Noumi for their valuable comments concerning the analysis and physics.

I would like to thank Prof .H. Tamura. He always taught physics to us in easy way to understand.

I would like to express my thanks to Dr. T. Takahashi and Dr. K. Tanida. I respect them not only as a physicist but also as a great programmer and engineer.

I am very thankful to Dr .P. K. Saha, Mr. J. H. Kim and Ms. M. Nakamura. They kindly taught me fundamental knowledge and technique of data analysis, programming and so on. I cannot imagine how much effort would have been required without their help.

I acknowledge the collaborators of the present experiment. Mr. B. H. Kang vigorously worked throughout the experiment. His contribution was essential especially in designing and constructing the decay counter. Ms. M. Kim and Ms. E. H. Kim. worked very hard in the preparation and data analysis. I spent nice days in KEK thanks to their warm heart and friendliness. Many discussions with Mr. Okada and Mr. Miyake very impressed me. They kindly answered my trivial questions even when they were very busy to write their master's theses. I am thankful to Dr. A. Toyoda and Mr. T. Maruta for their cooperations.

I am grateful to Dr .Y. Fujii and other members of Hashimoto Lab. for their valuable advises and assistances.

I also express my gratitude to Ms. M. Sekimoto, Mr. Y. Kakiguchi, and other staffs of SKS for their cooperations.

Bibliography

[1] M. M. Block, R. H. Dalitz, Phys. Rev. Lett. **11**, 96(1963).

[2] J. F. Dubach, Nucl. Phys. **A450**, 71c(1986).

[3] H. Bando, T. Motoba, J. Zofka, Int. J. Mod. Phys. Vol. 5, No. 21, 4021(1990).

[4] H. Noumi *et al.*, Phys. Rev. **C52**, 2936(1995).

[5] Y. Sato, Doctor thesis, Tohoku University(1998)

[6] Y. Sato *et al.*, Nucl. Phys. **A639**, 279c(1998).

[7] J. Szymanski *et al.*, Phys. Rev. **C43**, 849(1991).

[8] A. Ramos, M. J. Vicente-Vacas and E. Oset, Phys. Rev. C **55**, 735(1997)

[9] A. Parreno, A. Ramos, C. Bennhold, Phys. Rev. Lett. **C56**, 339(1997)

[10] S. Ajimura, Doctor thesis, Osaka University(1998).

[11] S. Ajimura *et al.*, Phys. Rev. Lett. **84**, 4052(2000).

[12] J. B. Adams, Phys. Rev. Lett. **156**, 1611(1967).

[13] I. Kumagai-Fuse, S. Okabe and Y. Akaishi, Phys. Lett. **B345**, 368(1995).

[14] T. Motoba, H. Bando, T. Fukuda and J. Zofka, Nucl. Phys. **A534** 597(1991).

[15] T. Motoba and K. Itonaga, Nucl. Phys. **A577** 293c(1994).

[16] H. Park *et al.*, Phys. Rev. **C61** (2000).

[17] H. Park, Doctor thesis, Seoul National University(1998).

[18] T. Inoue, S. Takeuchi and M. Oka, Nucl. Phys. **A597**, 563(1996).

[19] M. Oka, Nucl. Phys. **A639**, 317c(1998).

[20] K. Itonaga, T. Ueda and T. Motoba, Nucl. Phys. **A639**, 329c(1998).

[21] K. Itonaga, T. Ueda and T. Motoba, Nucl. Phys. **A691**, 197(2001).

[22] H. Outa *et al.*, Nucl. Phys. **A639**, 251c(1998).

[23] H. Outa, *Proposal for KEK-PS Experiment.*

[24] V. J. Zeps *et al.*, Nucl. Phys. **A639** 261c(1998).

[25] H. Hotchi, Doctor thesis, Tokyo University(2000).

[26] T. Hasegawa, Doctor Thesis, Tokyo University(1994).

[27] S. Okada, Master's thesis, Tokyo Inst. Tech.(2001).

[28] Y. D. Kim *et al.*, Nucl. Inst. and Meth. **A372** 431(1996).

[29] W. R. Leo, *Techniques for Nuclear and Particle Physics Experiments* (Springer-Verlag, 1992).

[30] Low Energy Particle Simulator: developed by M. Iwasaki.

[31] *ORBIT*: developed by S. Morinobu and T. Ichihara.

[32] O. Hashimoto *et al.*, Phys. Rev. Lett.**88**, (2002).

[33] J. H. Kim *et al.* to be published.

[34] K. Sasaki, T. Inoue and M. Oka, Nucl. Phys. **A669**, 331(2000).

[35] T. Jido, E.Oset and J. E. Palomar, Nucl. Phys. **A694**, 525(2001).